



Publication Year	2016
Acceptance in OA @INAF	2020-09-08T06:40:29Z
Title	Perspectives on Gamma-Ray Burst Physics and Cosmology with Next Generation Facilities
Authors	Yuan, Weimin; AMATI, LORENZO; Cordier, Bertrand; Gehrels, Neil; GHIRLANDA, Giancarlo; et al.
DOI	10.1007/s11214-016-0274-z
Handle	http://hdl.handle.net/20.500.12386/27193
Journal	SPACE SCIENCE REVIEWS
Number	202

Perspectives on Gamma-Ray Burst Physics and Cosmology with Next Generation Facilities

**Weimin Yuan · Lorenzo Amati · John
K. Cannizzo · Bertrand Cordier · Neil
Gehrels · Giancarlo Ghirlanda · Diego
Götz · Nicolas Produit · Yulei Qiu ·
Jianchao Sun · Nial R. Tanvir · Jianyan
Wei · Chen Zhang**

Received: date / Accepted: date

W. Yuan

Key Laboratory of Space Astronomy and Technology, National Astronomical Observatories
Chinese Academy of Sciences, Datun Rd 20A, Beijing 100012 China
E-mail: wmy@nao.cas.cn

L. Amati

INAF - IASF Bologna, via P. Gobetti 101
40129 Bologna, Italy
E-mail: amati@iasfbo.inaf.it

J.K. Cannizzo

CRESST/Joint Center for Astrophysics
Univ. of Maryland, Baltimore County
Baltimore, MD 21250, USA
E-mail: john.k.cannizzo@nasa.gov

B. Cordier

CEA-Irfu, Service d'Astrophysique
F-91191 Gif-sur-Yvette, France
E-mail: bertrand.cordier@cea.fr

N. Gehrels

Astroparticle Physics Division
NASA/Goddard Space Flight Center
Greenbelt, MD 20771, USA
E-mail: neil.gehrels@nasa.gov

G. Ghirlanda

Istituto Nazionale di Astrofisica INAF - Osservatorio Astronomico di Brera
Via E. Bianchi 46 - I 23807 Merate (LC), Italy
E-mail: giancarlo.ghirlanda@brera.inaf.it

D. Götz

CEA-Irfu, Service d'Astrophysique
F-91191 Gif-sur-Yvette, France
E-mail: diego.gotz@cea.fr

J. Sun

Institute of High-Energy Physics, Chinese Academy of Sciences,
Yuquan Lu 19B, Shijingshan District, Beijing, China
E-mail: sunjc@ihep.ac.cn

Abstract High-redshift Gamma-Ray Bursts (GRBs) beyond redshift ~ 6 are potentially powerful tools to probe the distant early Universe. Their detections in large numbers and at truly high redshifts call for the next generation of high-energy wide-field instruments with unprecedented sensitivity at least one order of magnitude higher than the ones currently in orbit. On the other hand, follow-up observations of the afterglows of high-redshift GRBs and identification of their host galaxies, which would be difficult for the currently operating telescopes, require new, extremely large facilities of at multi-wavelengths. This chapter describes future experiments that are expected to advance this exciting field, both being currently built and being proposed. The legacy of Swift will be continued by SVOM, which is equipped with a set of space-based multi-wavelength instruments as well as and a ground segment including a wide angle camera and two follow-up telescopes. The established Lobster-eye X-ray focusing optics provides a promising technology for the detection of faint GRBs at very large distances, based on which the THESEUS, Einstein Probe and other mission concepts have been proposed. Follow-up observations and exploration of the reionization era will be enabled by large facilities such as SKA in the radio, the 30m class telescopes in the optical/near-IR, and the space-borne WFIRST and JWST in the optical/near-IR/mid-IR. In addition, the X-ray and γ -ray polarization experiment POLAR is also introduced.

Keywords Gamma-ray bursts · high-redshift · Gamma-ray · X-ray · instrumentation

N. R. Tanvir
University of Leicester, Dept. of Physics and Astronomy,
University Road, Leicester, LE1 7RH, United Kingdom
E-mail: nrt3@le.ac.uk

N. Produit
ISDC, Chemin d' Ecogia 16, CH-1290 Versoix, Switzerland
E-mail: Nicolas.Produit@unige.ch

Y. Qiu · J. Wei · C. Zhang
Key Laboratory of Space Astronomy and Technology, National Astronomical Observatories
Chinese Academy of Sciences, Datun Rd 20A, Beijing 100012 China
E-mail: qiuy1@nao.cas.cn; wjy@nao.cas.cn; chzhang@nao.cas.cn

1 Introduction

Understanding the structure formation and the first stars around the epoch of reionization is a major driver for the next generation of space- and ground-based astronomical facilities. Being the brightest objects in the Universe, Gamma-Ray Bursts (GRBs) beyond redshift ~ 6 shine through the dark age as cosmic beacons and are thus potentially powerful probes of the distant early Universe. So far, seven GRBs with redshifts $6.2 - 9.4$ have been detected with the Swift satellite in its 10-year operation. New discoveries will continue to be made by the GRB mission SVOM in the foreseeable future, which is equipped with a set of space-based multi-wavelength instruments as well as a ground segment including a wide angle camera and two follow-up telescopes. Looking far into the future, a full exploration of the early Universe requires a much larger sample (~ 100) and events at even higher redshifts, i.e. redshift ~ 10 and beyond. This calls for the next generation of high-energy wide-field instruments with unprecedented sensitivity one order of magnitude or more higher than Swift/BAT. The proposed THESEUS and Einstein Probe missions (and others alike), which are based on novel technology of X-ray focusing, are promising concepts to achieve these goals. On the other hand, follow-up observations in multi-wavebands, particularly in the near- and mid-infrared, of the afterglows of high-redshift GRBs are key to identify their host galaxies, to measure the redshifts, and to enable detailed astrophysical and cosmological studies. This can be facilitated by the advent of the ground- and space-based large telescopes at multi-wavelengths currently being under construction, such as the 30-m class optical/near-IR telescopes, Square Kilometer Array (SKA) in the radio, and the space-borne WFIRST and JWST missions in the optical/near-IR/mid-IR. Last, complementary to the exploration of the early Universe, future extensive measurement of the X-ray and γ -ray polarization of GRBs, expected to be achieved by POLAR will open up a new dimension in understanding the radiation region geometry and radiation mechanism of GRB. This chapter describes future experiments that are expected to advance this exciting field, both currently being built and being proposed, including SVOM (Section 2; contributed by B. Cordier, D. Götz, Y. Qiu & J. Wei), POLAR (Section 3; J.C. Sun & N. Produit), WFIRST & JWST (Section 4; N. Gehrels & J.K. Cannizzo), TMT, GMT & E-ELT (Section 5; N. T. Tanvir), SKA (Section 6; G. Ghirlanda), Einstein Probe (Section 7; W. Yuan & C. Zhang), and THESEUS (Section 8; L. Amati).

2 SVOM

The success of the Swift mission for catching GRBs and other transients illustrates the benefit of its unique combination of space agility, fast communication with the ground, multi-wavelength observing capability, and long lifetime. These capabilities have permitted the detection of nearly 1000 GRBs and the measure of nearly 300 redshifts, have offered a new look at GRB progenitors and have led to several important discoveries, like the existence of GRBs at the epoch of the re-ionization of the universe. The aim of SVOM (Space-based multi-band astronomical Variable Objects Monitor) is to continue the exploration of the transient universe with a set of space-based multi-wavelength instruments, following the way opened by Swift. SVOM is a space mission developed in cooperation between the Chinese National Space Agency (CNSA), the Chinese Academy of Science (CAS) and the French Space Agency (CNES). The mission features a medium size satellite, a set of space and ground instruments designed to detect, locate and follow-up GRBs of all kinds, a anti-Sun pointing strategy allowing the immediate follow-up of SVOM GRBs with ground based telescopes, and a fast data transmission to the ground. The satellite (see Figure 1) carries two wide field high energy instruments: a coded-mask gamma-ray imager called ECLAIRS, and a gamma-ray spectrometer called GRM, and two narrow field telescopes that can measure the evolution of the afterglow after a slew of the satellite: an X-ray telescope called MXT and an optical telescope called VT. The ground segment includes additional instrumentation: a wide angle optical camera (GWAC) monitoring the field of view of ECLAIRS in real time during part of the orbit, and two 1-meter class robotic follow-up telescopes (the GFTs). SVOM has some unique features: an energy threshold of ECLAIRS at 4 keV enabling the detection of faint soft GRBs (e.g. XRFs and high-redshift GRBs); a good match in sensitivity between the X-ray and optical space telescopes which permits the detection of most GRB afterglows with both telescopes; and a set of optical instruments on the ground dedicated to the mission. The mission has recently been confirmed by the Chinese and French space agencies for a launch in 2021, and it has entered in an active phase of development. We present an overview of the scientific objectives of SVOM in the next sub-section, and a brief description of the instrumental aspects of the mission in the following ones.

2.1 Scientific objectives

The main science goal of SVOM is the study of cosmic transients detected in hard X-rays and in the optical domain. While the mission has been designed for the study of GRBs, it is also well suited for the study of other types of high-energy transients like Tidal Disruption Events (TDEs), Active Galactic Nuclei (AGNs), or galactic X-ray binaries and magnetars. For this type of sources, SVOM is both a "discovery machine", with wide field instruments that survey a significant fraction of the sky (ECLAIRS, GRM and GWAC), and a "follow-

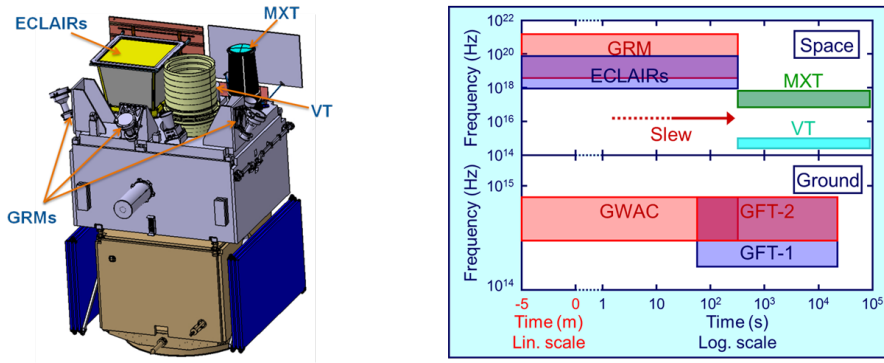


Fig. 1 Schematic showing the SVOM spacecraft with its multi-wavelength space payload. It consists of two wide-field instruments: ECLAIRs and the Gamma-Ray Monitor (GRM) for the observation of the GRB prompt emission and two narrow field instruments: the Micro channel X-ray Telescope (MXT) and the Visible Telescope (VT) for the observation of the GRB afterglow emission. Right: Space and ground instruments join to enable a unique coverage in time and wavelength.

up machine”, with fast pointing telescopes in space and on the ground (MXT, VT, and GFTs) that provide a multi-wavelength follow-up of different kinds of sources, with good sensitivity and a high duty cycle. The follow-up can be triggered by the satellite itself or from the ground, upon reception of a request for target of opportunity observations (ToO). In this section we concentrate on the objectives of SVOM for GRBs. Through GRB population simulations we have evaluated a GRB detection rate of 70–80 GRBs/yr for ECLAIRs and 90 GRBs/yr for GRM. One essential goal of SVOM is to provide GRBs with a redshift measurement. The redshift is required to measure the energetics of the burst and the epoch at which the GRB occurred in the history of the universe. Four elements in the design of the mission concur to facilitate the measure of the redshift for SVOM GRBs: a near anti-solar pointing during most of the orbit ensuring that SVOM GRBs can be quickly observed with ground based telescopes, a good sensitivity of the on-board optical telescope permitting the rapid identification of high- z candidates (which are not detected at visible wavelengths), Near Infra-Red follow-up on the ground to look for the afterglows of dark/high redshift GRBs, and agreements with the community to promote the optical spectroscopy of SVOM GRBs using large telescopes. With this strategy we expect to measure the redshift of more than 50% of SVOM GRBs, constructing a sample that could potentially be more representative of the intrinsic GRB population than the Swift sample. One drawback of this pointing strategy is that it avoids the galactic plane. Galactic sources can nevertheless be observed during target of opportunity pointings. In the following, we discuss a few selected topics about GRBs for which SVOM may bring decisive progress.

2.1.1 GRB Progenitors

In order to get a better understanding of the GRB phenomenon SVOM was designed to detect all kinds of GRBs, and to provide extensive multi-wavelength observations of the prompt GRB and its afterglow. In addition to classical long GRBs that will be detected by the two wide field instruments (ECLAIRs and GRM), SVOM will routinely detect short bursts with its gamma-ray monitor and soft GRBs (XRFs or highly redshifted GRBs) with ECLAIRs. The ability to detect soft GRBs with a spectral energy distribution (SED) peaking below 20-30 keV will favour the detection of X-ray flashes. As shown by BeppoSAX and HETE-2 (Heise et al. 2001; Sakamoto et al. 2004), these faint GRBs can only be detected if they are close enough and if their spectral energy distribution peaks at low energies (because faint GRBs with a SED peaking at high energies radiate too few photons to be detected). The detection of X-Ray Flashes in the local universe ($z < 0.1$) will permit detailed studies of their associated supernovae (as was the case for XRF 020903; Soderberg et al. 2005), providing crucial clues to understand the broader context of the SN-GRB connection.

2.1.2 GRB Physics

The instrument suite of SVOM will provide good multi-wavelength coverage of GRBs. For those occurring in the field of view of GWAC, the prompt emission will be measured from 1 eV to 5 MeV, with the GWACs, ECLAIRs, and the GRM. The prompt optical emission may also be observed by one GFT for GRBs lasting longer than 40 seconds. GRB afterglows will be observed with the two narrow field instruments on-board the satellite and with the ground follow-up telescopes on Earth. For some GRBs, SVOM will provide a very complete view of the phenomenon and its evolution, hopefully bringing new insight into the complex physics at work in these events. A lesson learned from Swift is that a few well observed GRBs may crucially improve our understanding of GRB physics, as was the case for GRB 130427, a bright nearby burst detected by Swift, Fermi and various optical and radio telescopes on the ground (Maselli et al. 2014; Perley et al. 2014). The physical processes at work within the jet remain not well understood even after the observation of hundreds of GRBs. Comprehensive discussions of the theoretical challenges connected with the understanding of the prompt GRB emission can be found in Kumar and Zhang (2015) and Zhang (2014). The authors show that several crucial questions connected to the physics of the ultra-relativistic jet and its interaction with the surrounding medium remain unanswered, like the nature and content of the jet (is the energy stored in the baryons or in magnetic fields?), the mechanisms of particle acceleration, the micro physics and the dominant radiation processes, the importance of the reverse shock, the role of pairs, etc. Performing multi-wavelength observations during the prompt emission and the early afterglow, SVOM will provide key observations to understand the physics of relativistic jets. GRBs detected with SVOM will also benefit from contemporaneous or

follow-up observations with a novel generation of powerful instruments, like CTA (the Cerenkov Telescope Array) for very high energy photons, LSST (Large Synoptic Survey Telescope) for optical transients associated with on-axis and off-axis GRBs, and the precursors of SKA (the Square Kilometer Array) in radio.

2.1.3 Cosmology

Their extreme luminosity of GRBs permits their detection in hard X-rays up to very high redshifts, possibly beyond $z = 10$ and the spectroscopy of the optical afterglow provides the redshift of the burst and a tomographic vision of the line of sight to the burst. With Swift and the measure of about 300 redshifts, GRBs are providing new diagnostics of the distant Universe. When the signal to noise ratio (SNR) of the optical spectrum of the afterglow is sufficient, we get detailed information on the circumburst medium, on the gas and dust in the host galaxy, on the intergalactic medium and the intervening systems. With a smaller SNR, the measure of the redshift allows locating the time of the explosion in the history of the universe and reconstructing the history of the GRB formation rate, which traces the formation rate of massive stars. There is of course a special interest in very distant GRBs ($z > 5$), which provide a unique view on the young Universe, especially since they occur in galaxies which are undetectable with other methods of observation. One exciting challenge of GRB missions is the detection of GRBs resulting from the explosion of population III stars (the first generation of stars formed with pristine gas containing no metals). Such events are expected to be rare, to occur at high redshifts, to have no detectable hosts (except in absorption in the spectrum of their optical afterglow) and afterglows that are only detectable in the near infrared. They could be similar to some very long GRBs found at lower redshift (Mészáros and Rees 2010; Gendre et al. 2013). We expect to detect about 5 GRBs/yr at redshift $z \lesssim 5$ with ECLAIRs, but they will be useful only if we can measure their redshift. One difficulty is that the optical afterglows of GRBs fade very quickly, and after a few hours they are often too faint to permit measuring the redshift of the burst. In order to quickly identify high- z candidates that deserve deep spectroscopy in the NIR, we rely on the sensitivity of VT and on fast NIR follow-up telescopes on the ground. Dark GRBs, whose afterglows are not detected in the VT, are good candidates for high- z bursts, but they can also be extinct by dust in the vicinity of the source. The nature of these events (distant or extinct GRB) will be confirmed quickly with fast visible/NIR photometry from the ground, allowing the most appropriate spectroscopic follow-up. In some cases, GRBs detected by SVOM could trigger follow-up observations by the JWST (James Webb Space Telescope) for the study of the hosts.

2.2 Space Borne Instruments

In this section and the following, we give a brief description of the instruments of SVOM. In order to be both a discovery machine and a follow-up machine, SVOM features two types of instruments: space based instruments and ground based instruments. We briefly describe these instruments below.

2.2.1 *ECLAIRs the hard X-ray coded mask imaging camera*

ECLAIRs (see Figure 2) is the instrument on-board the satellite that will detect and locate the GRBs. ECLAIRs is made of four parts: a pixellated detection plane (1024 cm^2) with its readout electronics, a coded mask, a shield defining a field of view of 2 steradians ($89^\circ \times 89^\circ$), and a processing unit in charge of detecting and locating transient sources. The detection plane is made of 200 modules of 32 CdTe detectors each, for a total of 6400 detectors of size $4 \times 4 \times 1 \text{ mm}$. Each module is read by a customized ASIC connected to an electronics that encodes the position, the time and the energy of each photon. One of the requirements of ECLAIRs is to reach an energy threshold of 4 keV, in order to study soft GRBs like X-Ray Flashes and highly redshifted GRBs. As shown in figure 2, the first modules satisfy the low energy threshold requirement (Godet et al. 2014). The coded mask is a square of side 54 cm located at a distance of 46 cm from the detection plane; it has an opening fraction of 40% and provides a localization accuracy of several arc minutes ($\sim 14'$ for a source at the limit of detection). The instrument features a count rate trigger and an image trigger, like Swift. These triggers are computed, from the photon data, in several energy bands and on time-scales ranging from 10 ms to several minutes. Our simulations show that ECLAIRs will detect 70-80 GRBs/yr.

2.2.2 *GRM: the Gamma-ray Monitor*

GRM consists of a set of three detection modules. Each of them is made of a scintillating crystal (sodium iodide), a photomultiplier and its readout electronics. Each detector has a surface area of 200 cm^2 and a thickness of 1.5 cm. One piece of plastic scintillator in front of NaI(Tl) is used to distinguish low energy electrons from normal X-rays. The three modules are pointed at different directions to form a total field of view of 2 sr, within which rough (of the order of 10 degrees radius) localization of transient sources can be achieved on-board. The energy range of the GRM is 15-5000 keV, extending the energy range of ECLAIRs towards high energies to measure E_{Peak} for a large fraction of SVOM GRBs. We expect that GRM will detect > 90 GRBs/yr. GRM will have a good sensitivity to short/hard GRBs, like the GBM of Fermi. GRM can generate on-board GRM-only triggers, taking use of only GRM detectors. Such triggers with localization information will be transferred to ECLAIRs for trigger enhancement on the short GRBs, and to ground facilities (e.g. GWAC, GW experiments) for joint observations. A calibration detector containing one

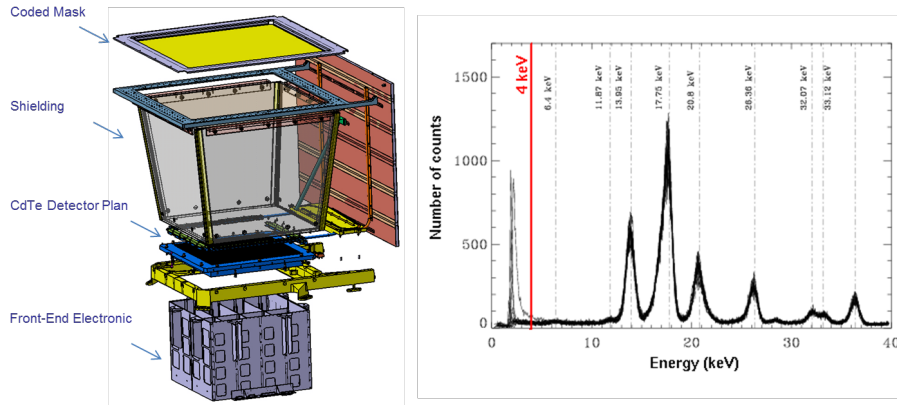


Fig. 2 Schematics showing the different sub-systems of ECLAIRs except the data processing unit in charge of the GRB detection and localisation. Right: Laboratory spectral measurements performed on a detector module prototype (a 32 CdTe pixel matrix) with radioactive sources (^{241}Am). The red vertical line corresponds to the expected low energy threshold of the ECLAIRs camera [6].

radioactive ^{241}Am isotope is installed on the edge of each detection module, for the purpose of gain monitoring and energy calibration. In addition, a particle monitor auxiliary to GRM can generate South Atlantic Anomaly alerts and help protecting the detection modules.

2.2.3 MXT: the Microchannel X-ray Telescope

MXT (see Figure 3) is a light and compact focusing X-ray telescope designed to observe and measure the properties of the GRB X-ray afterglow after a slew of the satellite. The telescope will implement a novel technique to focus X-rays, based on micropore optics arranged in a lobster eye geometry. The use of micropore optics instead of classical X-ray electro-formed mirrors permits a significant reduction of the size and weight of the telescope, fitting on a medium size satellite like SVOM. The optics has a diameter of 24 cm and a focal length of 1 meter (Götz et al. 2014). MXT will make use of the radiation hard pn-CCD detector developed for the DUO mission and adopted in a larger version for the eROSITA mission (Meidinger et al. 2014; Predehl et al. 2014). The MXT detector is made of 256×256 Si pixels of $75 \mu\text{m}$ side and has an expected energy resolution of 75 eV at 1 keV. MXT will be operated in the energy range of 0.2-10 keV, will have an effective area of 45 cm^2 at 1 keV, and a field of view of 64×64 arc minutes. Despite the smaller effective area with respect to XRT on board Swift at 1 keV (about 120 cm^2) MXT will be able to fully characterize the GRBs light curves (as shown in Figure 3). In fact with a sensitivity of $7 \times 10^{-13} \text{ erg cm}^{-2} \text{ s}^{-1}$ in 10^4 s , MXT will detect the afterglows of more than 90% of SVOM GRBs. Indeed its sensitivity is well adapted to early GRB afterglow observations, and its PSF of about 4 arc min will allow to significantly reduce the ECLAIRs error boxes. Simulations

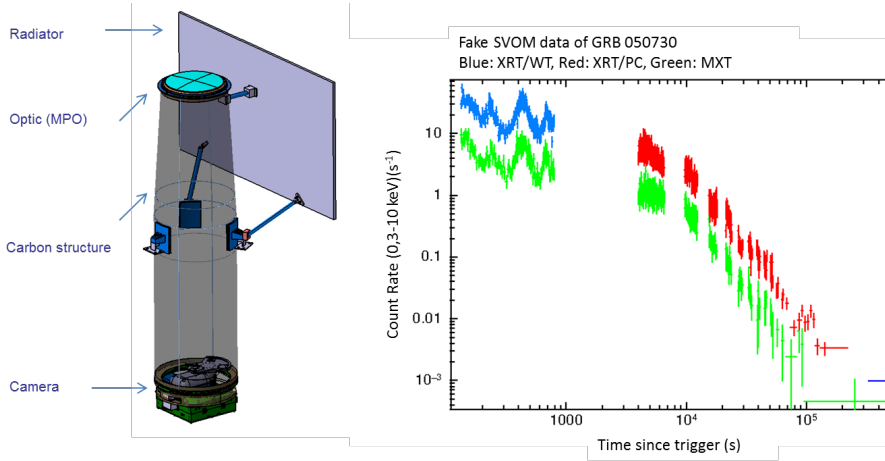


Fig. 3 Schematics showing the different sub-systems of the MXT. Right: XRT measured (blue and red points) versus MXT simulated (green points) light curve of GRB 050730, a GRB with a median flux in the Swift/XRT afterglow database.

based on the Swift-XRT database show that the localization accuracy for the MXT is $\sim 13''$ for 50% of the bursts, 10 minutes after the trigger (statistical uncertainty only).

2.2.4 VT: the visible Telescope

The Visible Telescope (VT) is a dedicated optical follow-up telescope on board the SVOM satellite. Its main purpose is to detect and observe the optical afterglows of gamma-ray bursts localized by ECLAIRs. It is a Ritchey-Chretien telescope (see Figure 4) with a diameter of 40 cm and an f-ratio of 9. Its limiting magnitude is about 22.5 (M_V) for an integration time of 300 seconds. VT is designed to maximize the detection efficiency of GRB's optical afterglows. Instead of a filter wheel, a dichroic beam splitter is used to divide the light into two channels, in which the GRB afterglow can be observed simultaneously. Their wavelength ranges are from $0.4\mu\text{m}$ to $0.65\mu\text{m}$ (blue channel) and from $0.65\mu\text{m}$ to $1\mu\text{m}$ (red channel). Each channel is equipped with a $2\text{k} \times 2\text{k}$ CCD detector. While the CCD for the blue channel is a normal thinned back-illuminated one, a deep-depleted one is adopted for the red channel to obtain high sensitivity at long wavelength. The Quantum Efficiency (QE) of the red-channel CCD at $0.9\mu\text{m}$ is over 50%, which enables VT to have the capability of detecting GRBs with the redshift larger than 6.5. The field of view of VT is about $26' \times 26'$, which can cover the error box of ECLAIRs in most cases. Both CCDs have a pixel size of $13.5\mu\text{m} \times 13.5\mu\text{m}$, corresponding to spatial resolutions of 0.77 arc second. This ensures the GRB positioning accuracy to be greatly improved by VT from several arc minutes (ECLAIRs) and tens of arc-seconds (MXT) to a level of sub-arc second.

In order to promptly provide the GRB alerts with the sub-arc second accuracy, VT will do some data processing on board. After a GRB has been localized by the co-aligned MXT, lists of sources are extracted from the VT sub-images whose centres and sizes are determined by the GRB positions and the corresponding error boxes provided by MXT. The lists are immediately downlinked to the ground through the VHF network. Then, the ground software will make finding charts with these lists (see Figure 4) and search the optical counterparts of the GRB by comparing the lists with the existing catalogues. If a counterpart is identified, an alert will be then produced and distributed to world-wide astronomical community, which is useful for triggering large ground-based telescopes to measure the redshifts of the GRBs by spectroscopy. VT is expected to do a good job on detecting high-redshift GRBs. The confirmed high-redshift GRBs are rare in the Swift era, in contrast to a theoretical prediction of a fraction of more than 10% (Salvaterra 2015). This is probably due to the fact that for most Swift GRBs the early-time optical imaging follow-up is not deep enough for a quick identification and some faint GRBs cannot be spectroscopically observed in time by the large ground-based telescopes. This passive situation will be significantly improved by SVOM, due to the high sensitivity of VT, in particular at long wavelength, and the prompt optical-counterpart alerts. Additionally, the anti-solar pointing strategy of SVOM allows GRBs to be spectroscopically observed by large ground-based telescopes at the early time of the bursts. Consequently, more high-redshift GRBs are expected to be identified in the SVOM era. VT is also used to support the platform to achieve the required high pointing stability. A Fine Guidance Sensor (FGS) is mounted on the VT focal plane to measure relative image motions. Its images are processed in real time by a specialized data processing unit to get the centroid positions of several stars brighter than the magnitude of 15 (M_V). The results are sent at a frequency of 1Hz to the platform to improve the pointing stability, which enables VT to have a good performance in a long exposure time.

2.3 Ground Based Instruments

The ground follow-up instruments constitute an important part of the mission. Three instruments are developed for the follow-up of SVOM GRBs: a wide angle camera that surveys a significant fraction of the sky for transients, and two robotic telescopes. In addition to these dedicated instruments, the SVOM collaboration will seek agreements with various existing telescopes or networks willing to contribute to the follow-up of SVOM GRBs.

2.3.1 GWAC: the Ground Wide Angle Camera

GWAC (see Figure 5) provides a unique way to survey a large field of view for optical transients. The instrument will monitor 63% of ECLAIRs field of view, looking for optical transients occurring before, during and after GRBs. GWAC

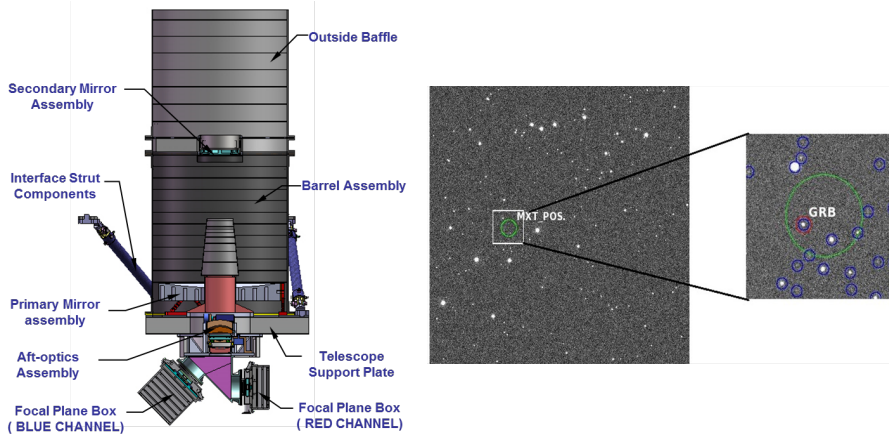
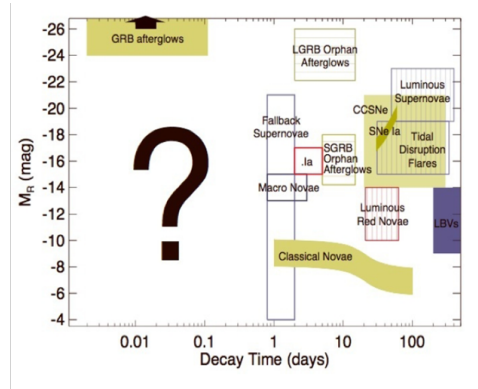


Fig. 4 Schematic showing the different sub-systems of the VT. Right: a simulated image of the VT and its associated finding chart.



Wozniak et al. 2009

Fig. 5 First prototype of one GWAC module. The final system will be composed by 9 modules. Right: the figure shows the discovery space of an instrument dedicated to short time-scale optical transients (Wozniak et al. 2009).

will also have its own trigger system, providing alerts to the world. GWAC is a complex system: the heart of the system is a set of 36 wide angle cameras with a diameter of 18 cm and a focal length of 22 cm, together these cameras cover a field of view of 5000 sq. deg. They use $4k \times 4k$ CCD detectors, sensitive in the range of wavelength 500-800 nm. These cameras reach a limiting magnitude $V=16$ (5σ) in a typical 10 second exposure. This set of cameras is completed by two 60 cm robotic telescopes. equipped with EMCCD cameras. These telescopes will provide multicolour photometry of the transients discovered by GWAC with a temporal resolution ≤ 1 second.

2.3.2 GFTs: the Ground Follow-up Telescopes

The ground follow-up telescopes have two main goals. Firstly, they measure the photometric evolution of the optical afterglow in the first minutes after the trigger in a broad range of visible and NIR wavelengths, with a temporal resolution of few seconds. Secondly, when an afterglow is detected, they provide its position with arc second precision within 5 minutes of the trigger. Some essential features of the GFTs are their field of view, their size, and their sensitivity in the near infrared. The field of view (~ 30 arc minutes) enables observing quickly the entire error boxes of ECLAIRs. The size, typically 1 meter, allows the detection of all visible (i.e. non-dark) afterglows at the condition to arrive within few minutes after the trigger (Akerlof and Swan 2007; Klotz et al. 2009). Finally, the near infrared sensitivity permits the detection of high- z GRBs and GRBs extinct by dust, whose afterglow are obscured in the visible domain (Greiner et al. 2008). GFTs are especially useful for the study of the early afterglow during the slew of the satellite, and for the rapid identification of the optical afterglow in various cases: when SVOM cannot slew to the burst or when the slew is delayed due to pointing constraints, and when the optical afterglow is only visible in the NIR. One telescope is located in China at Xinglong Observatory and the other one will be located in Mexico at San Pedro Mártir.

2.4 The System

In order to facilitate measuring the redshifts of GRBs detected with ECLAIRs, the instruments of SVOM will be pointed close to the anti-solar direction. Most of the year the optical axis of the SVOM instruments will be pointed at about 45° from the anti-solar direction. This pointing is interleaved with avoidance periods during which the satellite passes away from the Sco X-1 source and the galactic plane. This strategy ensures that SVOM GRBs will be in the night hemisphere and quickly observable from the ground by large telescopes. More details on the SVOM pointing strategy, can be found in Cordier et al. (2008).

As soon as a GRB will be located, its coordinates and its main characteristics will be sent to the ground within seconds with a VHF antenna. The VHF signal will be received by one of the ~ 40 ground stations distributed around the Earth below the orbit. The data will then be relayed to the Operation Center, which will send SVOM alerts to the internet via the GCN and VO Event networks (<http://gcn.gsfc.nasa.gov/>), and to the ground instruments GWAC and the GFTs. SVOM can also perform target of opportunity observations (with MXT and VT for instance), with a delay of few hours, which depends on the availability of uplink communication with the satellite.

SVOM will try to select high- z GRB candidates by analysing MXT and VT data, and multi-band photometry data from GFTs. If a GRB is detected by MXT in the soft X-rays, but not by VT in the optical band, it will be selected as a candidate of high- z or an optically dark GRB. Ground telescopes

with NIR capabilities are encouraged to follow up these candidates as soon as possible to try to measure their redshift. GFTs will be able to measure photometric redshifts by observing GRB afterglows with multiple filters from the visible to the NIR bands.

2.4.1 Conclusion

SVOM will be a highly versatile astronomy satellite, with built-in multi-wavelength capabilities, autonomous re-pointing and dedicated ground follow-up. With its peculiar pointing strategy and the low energy detection threshold, SVOM is expected to improve the number of GRBs detected at high redshift, and hence to contribute to the use of GRBs as probes of the young Universe.

Beyond the GRB studies emphasized here, SVOM will bring new observations about all types of high energy transients, in particular those of extragalactic origin (TDEs, AGNs, etc.).

3 POLAR - Space-Borne Gamma-Ray Bursts Compton Polarimeter

Until recent years, only a few polarization measurement results on Gamma-Ray Burst (GRB) prompt emissions have been published (Yonetoku et al. 2011), while in the same time more and more hard X-ray/Gamma-ray polarization measurement instruments have been put into operation or under development. All these efforts will accumulate a larger observation database on GRB's polarization.

POLAR (Produit et al. 2005) is a novel space-borne Compton polarimeter dedicated for the precise measurement of the polarization of GRB's prompt emission, which is expected to be on-board the Chinese space laboratory "Tiangong-2 (TG-2)" with a scheduled launch date in late 2016. The future detailed measurement of the polarization of GRBs will lead to a better understanding of its radiation region geometry and emission mechanisms. POLAR will contribute greatly to two aspects on the polarization observation of GRBs. One is its high sensitivity which is minimum detectable polarization (MDP). The MDP of POLAR can be as low as $\sim 10\%$ (Suarez 2010). The other one is its high observation statistics. ~ 50 GRBs/year are expected to be detected by POLAR. This will provide significant results for restricting the radiation mechanism of GRBs.

3.1 Design of POLAR detector

POLAR is composed of the polarization detector (OBOX) and electronic cabinet (IBOX). OBOX consists of 25 detector modular units (DMU). Each DMU is composed of 64 low-Z material plastic scintillator (EJ-248M) bars, read-out by a flat-panel multi-anode photomultipliers H8500 and ASIC front-end electronics. The CAD view of DMU and OBOX are shown in Figure 6

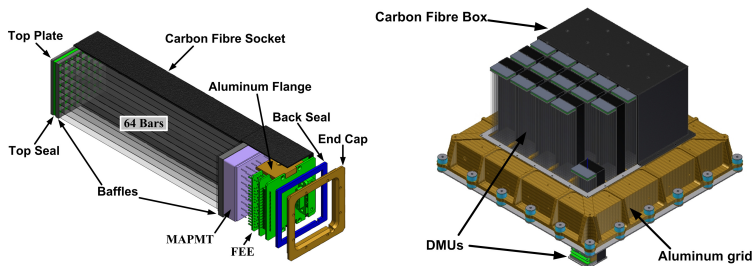


Fig. 6 Detector design of POLAR. Left: Detector modular unit; Right: polarization detector OBOX

The linear polarization degree and polarization direction of the polarized Gamma-rays can be reconstructed by POLAR through Compton scattering effect. In order to improve the Compton scattering efficiency, the low-Z material plastic scintillator has been selected as the detection material of POLAR as it is more stable chemically and mechanically.

3.2 Detection principle

The main interaction between the hard X-rays/Gamma-rays within the energy range 50 keV~500 keV and plastic scintillator material is Compton scattering. The differential cross-section is given by the Klein-Nishina formula for the polarized Compton scattering interaction process:

$$\begin{aligned} \frac{d\sigma_p}{d\Omega} &= \frac{r_0^2}{2} \varepsilon^2 [\varepsilon + \varepsilon^{-1} - 2 \sin^2 \theta \cos^2 \eta] \\ &= \frac{r_0^2}{2} \varepsilon^2 [\varepsilon + \varepsilon^{-1} - \sin^2 \theta + \sin^2 \theta \cos(2(\eta + \frac{\pi}{2}))], \end{aligned} \quad (1)$$

where r_0 is the classic radius of an electron and $\varepsilon=E'/E$ is the ratio of the energy of the scattered photon and the energy of the incident photon, θ is the Compton scattering angle and η is the scattering azimuth angle.

An incident photon interacts with one of the 1600 PS bars in POLAR through Compton scattering effect; the recoil electron will be absorbed by the PS bar and its deposited energy will be detected by POLAR and readout by the following electronics. The scattered photon will interact with next PS bars until being absorbed or escaping the detector array. For the unpolarized Gamma-rays, the scattering azimuth angle is isotropic, while for the polarized Gamma-rays, the scattering azimuth angle distribution is related to the incident photons' polarization degree and polarization angle. Therefore, the polarization property of the incident Gamma-rays can be reconstructed by analyzing the distribution of the Compton scattering azimuth angles. Figure 7 shows the detection principle of POLAR.

In Figure 7, \mathbf{P} is the polarization vector of the incident Gamma-rays, θ_γ and φ_γ describe the incident photons' direction, e^- is the recoil electron, ξ is the projection of the Compton scattering azimuth angle in the detector plane.

3.3 Physics performance study with Monte-Carlo method

The performance of POLAR has been studied using the Monte-Carlo simulation method. The GEANT4 toolkit is used for the simulations. The Band

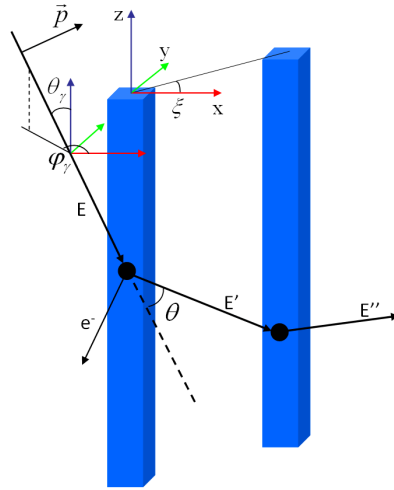


Fig. 7 Detection principle of POLAR by Compton scattering effect

(Band et al. 1993) function is used to create the spectrum of an GRB. Typically, the standard GRB spectrum ($\alpha=-1.0$, $\beta=-2.5$ and $E_{peak}=200$ keV) is used for the study. Figure 8 shows the triggered events on the 1600 detection channels of POLAR with different GRB incident angles.

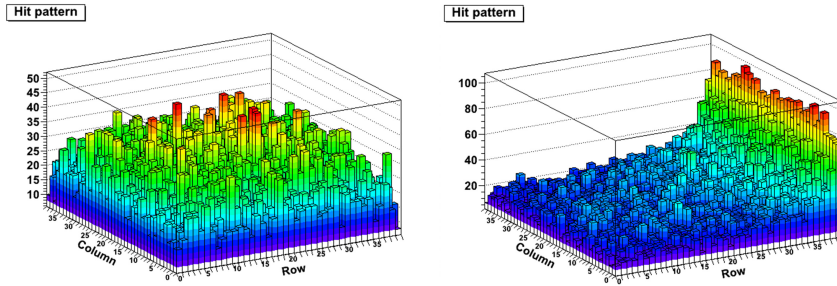


Fig. 8 Triggering pattern of POLAR detector with standard incident GRB photons. Left: $\theta_\gamma=0^\circ$, $\varphi_\gamma=0^\circ$; Right: $\theta_\gamma=45^\circ$, $\varphi_\gamma=0^\circ$

For different incident angles of GRBs, the reconstructed modulation factor by POLAR can be quite different. Figure 9 shows the modulation factor measured by POLAR as a function of the incident angle of GRB when the GRB photons are 100% polarized. More simulation results are discussed elsewhere (Suarez 2010; Xiong et al. 2009; Sun 2012).

3.4 Calibration tests

In 2015, the full flight model of POLAR has been constructed. A series of calibration activities have been performed to verify the basic working function of the instrument, test and optimize its working parameters, study the polarization measurement performance of the detector, verify and improve the data analysis procedure and algorithm, as well as to optimize the Monte-Carlo simulation model of POLAR which will be used in the in-orbit data analysis. Among all of the calibration tests, the most important one is the polarization measurement of POLAR performed with the European Synchrotron Radiation Facility (ESRF) beam. The beamline used for the test is ID11 which can provide us with 100% polarized hard X-rays between 35 keV~140 keV. The beam of ID11 is horizontally polarized. The size of the beam used for POLAR calibration is 0.5×0.5 mm² with original beam intensity $\sim 10^7$ phs/s, which was reduced to about $10^3 \sim 10^4$ phs/s with absorber to avoid the data pileup in the electronics.

During the ESRF beam test, four different beam energies were used, i.e., 140 keV, 110 keV, 80 keV and 60 keV. For each beam energy, three different beam incident angles (0° , 30° and 60°) were chosen, where 0° is on-axis, 30° and 60° are off-axis. Figure 10 shows the very preliminary analysis results of the reconstructed Compton scattering azimuth angle distributions (modulation curves) with 140 keV beam. When fitting the modulation curves, the calculated modulation factors for 90° and 0° polarized beam are $40.23\% \pm 0.0039\%$ and $39.31\% \pm 0.0038\%$, respectively. The measurement results are quite similar

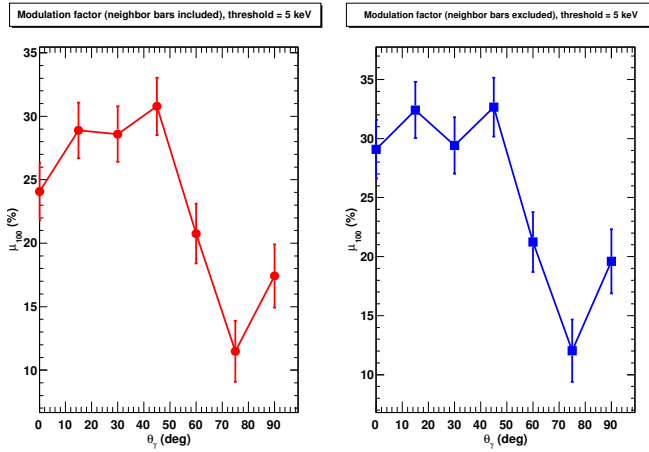


Fig. 9 Simulated modulation factor (100% polarized) as a function of the incident angle θ_γ of GRB; φ_γ is set to 0° for simplicity. Left: neighboring bars included; Right: neighboring bars excluded

to the Monte-Carlo simulation result of 40.90%, which verifies the accuracy of the model for the Monte-Carlo simulations.

3.5 Summary and discussions

For GRB prompt emissions, the most interesting energy range is about 100 keV~200 keV, within which POLAR has its best performance. The Monte-Carlo simulation results show that for the GRBs with total energy fluence F_{total} larger than 3×10^{-5} erg·cm $^{-2}$, the minimum detectable polarization (MDP) of POLAR can reach below $\sim 10\%$. In addition, for strong GRBs POLAR can localize their positions with accuracy better than 5° ($F_{\text{total}} \geq 10^{-5}$ erg·cm $^{-2}$). The main technical properties of POLAR are summarized in Table 1. The calibration test results show that POLAR performs as expected on the polarization measurement. After eliminating all kinds of system effects of the instrument during the data analysis procedure and optimising the Monte-Carlo simulation model, the final measurement results and simulation results are quite similar. The calibration results as well as the optimised instrument working parameters will be used in the further Monte-Carlo simulations and real in-orbit operations.

POLAR has also undergone and passed the space qualification tests, such as thermal cycling, vibration, shock and thermal vacuum, etc. These tests can verify the reliability of POLAR instrument and guarantee its long-term operation and observation.

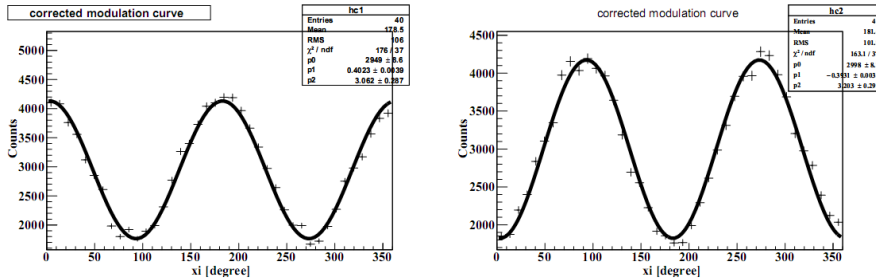


Fig. 10 Modulation curve measured during the ESRF beam tests. Left: the polarization direction of the beam relative to POLAR detector is 90° ; Right: the polarization direction of the beam relative to POLAR detector is 0°

Table 1 Main technical properties of POLAR

No.	Property	Performance
1	Detector material	Plastic scintillator (EJ-248M)
2	Yearly detectable GRBs	~ 50
3	GRB localization accuracy	$\leq 5^\circ$ ($F_{\text{total}} \geq 10^{-5}$ erg·cm $^{-2}$)
4	Detection energy range	50 keV \sim 500 keV
5	Field of view	$\pm 70^\circ \times \pm 70^\circ$
6	Minimum detectable polarization	$< 10\%$ ($F_{\text{total}} \geq 3 \times 10^{-5}$ erg·cm $^{-2}$)

4 *WFIRST* and *JWST*

4.1 *WFIRST*

4.1.1 *Instrumentation*

WFIRST consists of two instruments, a Wide-Field Instrument (WFI) and a coronagraph.

The WFI will be capable of imaging and spectroscopy over thousands of square degrees and monitoring of SNe and microlensing fields. It has sensitivity in the $0.7 - 2\mu\text{m}$ bandpass and a 0.28 deg^2 field-of-view (FOV), about a hundred times that of *JWST*. The WFI has 18 H4RG¹ detectors (288 Mpixels) and utilizes 6 filter imaging. The wide field instrument includes two channels, a wide field channel and an integral field unit (IFU) spectrograph channel. The wide field channel includes three mirrors and a filter/grism wheel to provide an imaging mode covering $0.76 - 2.0 \mu\text{m}$ and a spectroscopy mode covering $1.35 - 1.95 \mu\text{m}$. The IFU channel uses an image slicer and spectrograph to provide individual spectra of each 0.15 arcsec wide strip covering the $0.6 - 2.0 \mu\text{m}$ over a $3.00 \times 3.15 \text{ arcsec}$ FOV.

The coronagraph can image ice and gas giant exoplanets as well as debris disks. It has a $400 - 1000 \text{ nm}$ bandpass, $\leq 10^{-9}$ contrast, and a 100 msec inner working angle (at 400 nm). The coronagraph instrument includes an imaging mode and a spectroscopic mode to perform exoplanet direct imaging and spectroscopic characterization of planets and debris disks around nearby stars.

4.1.2 *Science*

WFIRST has a 2.4 m wide-field IR telescope ($0.7 - 2 \mu\text{m}$) and an exoplanet imaging coronagraph instrument ($400 - 1000 \text{ nm}$). It will (i) carry out galaxy surveys over thousands of square degrees down to $J = 27 \text{ AB}$ to study dark energy (Figure 11) weak lensing and baryon acoustic oscillations, (ii) monitor a few square degrees for dark energy SN Ia studies, (iii) perform microlensing observations of the galactic bulge for an exoplanet census, and (iv) undertake direct imaging observations of nearby exoplanets with a pathfinder coronagraph. The mission will have a robust and well-funded guest observer program for 25% of the observing time. With a $< 1 \text{ hr}$ TOO response time (TBD, under study), *WFIRST* will be a powerful tool for time domain astronomy and for coordinated observations with gravitational wave experiments. Gravitational wave events produced by mergers of nearby binary neutron stars (LIGO-Virgo, cf. Kanner et al. 2012) or extragalactic supermassive black hole binaries (*LISA*) will produce electromagnetic radiation that *WFIRST* can observe.

¹ H4RG is a hybrid CMOS (Complimentary Metal-Oxide-Semiconductor) $4\text{K} \times 4\text{K}$ optical imager made by Teledyne Scientific & Imaging.

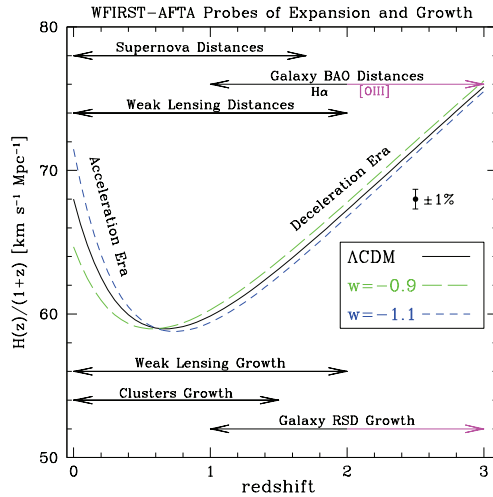


Fig. 11 Dark energy techniques used by *WFIRST* (Spergel et al. 2015).

4.2 *JWST*

4.2.1 Instrumentation

The Integrated Science Instrument Module (ISIM) will house the four main instruments that will detect light from distant stars and galaxies, and planets orbiting other stars. The ISIM will include:

- (i) the Near-Infrared Camera, or NIRC*am* (University of Arizona),
- (ii) the Near-Infrared Spectrograph, or NIR*Spec* (ESA, with components provided by NASA/GSFC),
- (iii) the Mid-Infrared Instrument, or MIRI (European Consortium, European Space Agency (ESA), and NASA Jet Propulsion Laboratory),
- and (iv) the Fine Guidance Sensor/ Near InfraRed Imager and Slitless Spectrograph, or FGS/NIR*ISS* (Canadian Space Agency).

The 6.5 m primary mirror, a gold-coated beryllium reflector, will have a collecting area about five times that of *HST*. *JWST* will be oriented towards near-IR astronomy, but with sensitivity also in orange and red light, as well as the mid-IR. Its coverage will span 0.6–27 μm . The motivation for an emphasis on near-IR to mid-IR is three-fold: high- z objects have their visible emissions shifted into the IR, cold objects such as debris disks and planets emit most strongly in the IR, and this band has been difficult to study from the ground or by previous space missions.

JWST will operate near the Earth-Sun L2 Lagrange point, $\sim 1.5 \times 10^{11}$ m beyond the Earth. Objects near this point can orbit the Sun synchronously with the Earth, allowing the telescope to remain at a roughly constant distance, using a single sunshield to block heat and light from the Sun and Earth.

This will keep the temperature of the spacecraft below 50 K which is necessary for IR observations.

Launch is scheduled for 2018 on an Ariane 5 rocket. Its nominal mission length is five years, with a goal of ten years.

4.2.2 Science

JWST's scientific mission has four main components: (i) to search for light from the first stars and galaxies, (ii) to study the formation and evolution of galaxies, (iii) to understand the formation of stars and planetary systems, and (iv) to study planetary systems and the origins of life. This science will be facilitated by *JWST*'s near-IR capabilities.

JWST is expected to see the very first galaxies, forming just a few 100 Myr after the Big Bang. IR observations allow the study of objects and regions of space which would be obscured by gas and dust in the visible, such as the molecular clouds where stars are born, the circumstellar disks that give rise to planets, and the cores of active galaxies. Relatively cool objects emit primarily in the IR. Most objects cooler than stars are better studied in the IR, including ISM clouds, brown dwarfs, planets – both in our own and other solar systems, and comets and Kuiper belt objects. In addition, *JWST* will be a valuable tool in high- z GRB follow-up (Figure 12) thanks to its ability to see back to early time.

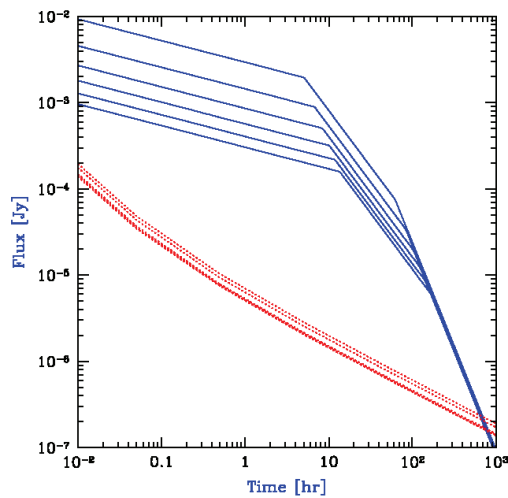


Fig. 12 Detectability of high- z GRB afterglows versus observer time $t - T_0$ (Bromm & Loeb 2007; from Barkana & Loeb 2004). GRB afterglow light curves are presented at the redshifted $\text{Ly}\alpha$ wavelength (solid blue curves). *JWST*/NIRSpec detection threshold (dotted red curves) are shown adopting a spectral resolution $\lambda/\Delta\lambda = 5000$, a signal to noise ratio of 5 per spectral resolution element, and an exposure time of $0.2(t - T_0)$. For each set of curves $z = 5, 7, 9, 11, 13, \text{ and } 15$, respectively (top to bottom).

4.3 Summary

JWST and *WFIRST* will bring in a new era of NIR and MIR astrophysics. *JWST* will provide very deep ($J = 29$) observations with multiple instruments. *WFIRST* will provide wide-field (1000's of square degrees) deep ($J = 27$) surveys. For both missions GRB follow-up science will be an integral part of science programs; *JWST* will have a 2 d TOO response time, while *WFIRST* will have a < 1 hr response time. TOO follow-ups for both missions will be limited to few per year.

5 The 30 m class ground-based telescopes

5.1 Introduction

As of 2015, construction has begun for three giant 30 m class ground-based optical/infra-red telescopes: the Giant Magellan Telescope (GMT) at Las Campanas, Chile, the Thirty Meter Telescope (TMT) at Mauna Kea, Hawaii, and the European Extremely Large Telescope (E-ELT) at Cerro Armazones, also in Chile. Thus by 2025 it is expected astronomers will have access to facilities significantly more powerful than the existing state-of-the-art 8 m generation. Their advantage goes beyond simply enhanced light-gathering-power, since each telescope is also planned to have sophisticated capabilities for high-order adaptive optics, thus providing spatial resolutions even better than the space-based *HST* and *JWST* for many observations (e.g., Gilmozzi and Spyromilio 2007). A summary of the basic vital statistics for each telescope is given in Table 2.

Table 2 Summary of planned 30 m class telescope characteristics

Telescope	Location	Altitude (m)	Diameter (m)	Mirror technology
GMT	Las Campanas	2550	24.5	7 monolithic mirrors, common focus
TMT	Mauna Kea	4050	30	Segmented primary
E-ELT	Cerro Armazones	3060	39.3	Segmented primary

A major driver for construction of these facilities is the exploration of early structure formation, during and before the epoch of reionization. This pushes towards optimisation in the near infra-red, since the Gunn-Peterson trough renders the universe opaque at rest-frame wavelengths below 1215Å, which corresponds to $\lambda > 1 \mu\text{m}$ at $z \gtrsim 7$. In recognition of this, all three telescope consortia have prioritised building of intermediate resolution, integral field spectrographs with nIR capability; namely HARMONI on the E-ELT, IRIS on the TMT and GMTIFS on the GMT. HARMONI and IRIS, indeed, have been selected as first light instruments. With spectral resolutions of $R \sim 4000\text{--}10000$, the majority of the available spectral range is between bright night-sky lines, and therefore provides low background and consequently high sensitivity.

5.2 High redshift transient science

5.2.1 Science drivers

Gamma-ray bursts are extremely bright, and hence visible in principle to very high redshifts. This, combined with their very broad spectral energy distributions, and association with massive star death, has long been recognised as

making them potentially very powerful probes of the early universe (Lamb and Reichart 2000; Tanvir and Jakobsson 2007). They trace early star formation, pin-point the positions of primeval galaxies, and provide luminous backlights for absorption spectroscopy (Chornock et al. 2013; Sparre et al. 2014; Hartoog et al. 2015).

To-date, the highest spectroscopic redshift for a GRB is $z = 8.2$ for GRB 090423 (Tanvir et al. 2009), whilst a photometric redshift of $z \approx 9.4$ was found for GRB 090429B (Cucchiara et al. 2011). However, despite their high intrinsic luminosities, at these distances follow-up with the current generation of telescopes and instruments is hard for all but the most extreme events. Thus it is likely that some high- z GRBs detected by *Swift* have not been recognised as such, and those that have been recognised have usually lacked the high-S/N data to fully exploit their potential.

The next generation telescopes combine near infra-red optimisation with exquisite point-source sensitivity, thanks to their large collecting area and AO-assisted high spatial resolution. Thus afterglows for which only redshifts could be obtained previously, will in the future be used to study abundances, neutral hydrogen, dust and molecular content in even very faint hosts. All of these properties are extremely difficult to study by other means. This potential is illustrated graphically in Figure 13, which shows a simulated E-ELT spectrum of a typical GRB afterglow at $z = 8.2$ (in fact based on observed luminosity of GRB 090423). The measurement of HI column in both host and intergalactic medium (IGM) in a statistical sample of high- z afterglows would be of considerable importance in understanding the sources driving reionization. The former provides the distribution of opacities, and hence escape fractions for ionizing radiation, along the lines of sight to massive stars in the early universe (Chen et al. 2007; Fynbo et al. 2009), while the latter would allow us to map the progress of reionization and its variation from field to field (McQuinn et al. 2008).

Other transients that may be studied by 30 m class telescopes include supernovae of all types, particularly superluminous supernovae that, although rare, are bright enough to be studied in detail at $z > 6$. This class of event may include pair-instability supernovae, the likely end-point of many massive population III stars (Heger et al. 2003).

5.2.2 Challenges

Observing transients with 30 m class telescopes offers great promise, but also presents particular challenges. Some challenges are for the wider astronomical community, in particular it is obviously essential that we maintain a capability to discover transient sources to feed into down-stream follow-up. In the 2020s new sources of transient discovery should be operating, notably the Large Synoptic Survey Telescope (LSST), the advanced generation gravitational wave detectors (e.g., aLIGO, aVirgo), and the SVOM satellite. However, of these only SVOM will be capable of detecting high redshift sources, specifically gamma-ray bursts (GRBs) and related high-energy transients. Since SVOM's

z=8.2 simulated E-ELT afterglow spectra

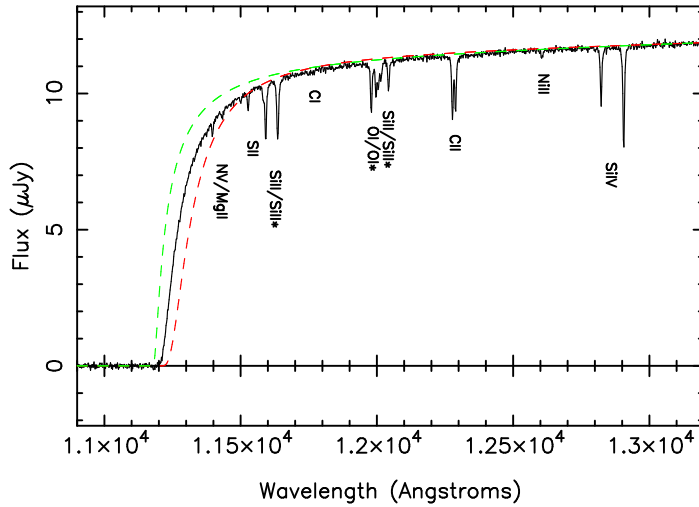


Fig. 13 Simulated spectrum (black solid curve) of typical GRB afterglow around the Ly- α line, as it would be seen in a 30 min exposure with E-ELT. The high signal-to-noise allows precise determination of neutral hydrogen column in both the host and intervening intergalactic medium, together with abundances for many metal species (the simulation is of 1% of Solar metallicity). Attempts to fit the damping wing with a host HI only model is shown by the red dashed curve, and a 100% neutral IGM only model as a green dashed curve; both provide poor fits. This shows that with such S/N it is possible to decompose the host HI column density and IGM neutral fraction.

capabilities are broadly similar to those of *Swift* we still only expect a modest rate of high- z bursts to be detected. Another challenge for transient follow-up, particularly of GRBs, is that their rapid time-evolution means that observations should ideally be done on a time-scale of hours after trigger. With the 30 m telescopes being restricted to just two geographical regions of the Earth, this limits the potential for follow-up, and, especially if one also considers weather and technical down-time, strongly motivates the continued operation of smaller telescopes as part of a transient follow-up network.

Several other challenges are at least more within the control of the consortia building the 30 m class telescopes. First and foremost is the provision of suitable imaging and spectroscopic capability. Unlike some other areas of astronomy, wide field is not key here, but good spatial resolution and (simultaneous) wide wavelength coverage is important. Since speed is of the essence, operational efficiency is also very important, both to realise rapid responses to trigger requests (quick instrument/mode changes, active optics reconfiguring, target acquisition, etc.), and also to expedite quick-look reduction and transmission of data to observers (or their software agents) allowing further

follow-up to be initiated with minimal delay. These capabilities require attention even in the design phase, for example to ensure that suitable data calibration products will exist to support the desired quick-look pipeline processing.

5.3 Host galaxies

In addition to the transients themselves, the 30 m class telescopes will provide unprecedented insights into their host galaxies. In general, high- z galaxies found in Lyman-break surveys are compact (e.g., Curtis-Lake et al. 2014), typically a few tenths of an arcsec, and hence only crudely resolved at *HST* resolution in the nIR. GRB hosts seem to be even fainter (Tanvir et al. 2012), and probably smaller, but with with spatial resolutions as good as ~ 0.04 arcsec for E-ELT, significant detail will be resolvable, allowing us to see probe the physical conditions leading to early star formation.

5.4 Conclusions

Within ten years, if these ambitious plans come to fruition, the astronomical community will have access to three 30 m class telescopes. Thanks to their huge grasp, adaptive optics capability, and near-infrared optimisation, these facilities will revolutionise our view of early structure formation in and before the era of reionization. Observations of transients and their host galaxies has a particularly important role to play, as they provide a route to studying in remarkable detail the physical nature of the very small star-forming galaxies that are thought to have dominated star formation at that time.

6 Radio observations of GRBs and orphan afterglows

6.1 Radio observations of GRBs

Radio observations of GRBs dates back to the end of the nineties when the afterglow discovery (Costa et al. 1997; van Paradijs et al. 1997) opened a new era in the field of GRBs with the follow up of their long wavelength long lasting afterglow emissions. The study of X-ray and optical emission from GRBs was revolutionised, starting in 2005, by the Swift satellite (Gehrels et al. 2009) thanks to its fast (within one minute) pinpointing (with subarcmin precision) of the location of the γ -ray event. Currently, $\sim 95\%$ of the bursts detected by the γ -ray detector (BAT – Burst Alert Telescope – 15–150 keV) are detected on board by the X-Ray Telescope (XRT; 0.1–3 keV) and $\sim 75\%$ of these are also detected at optical wavelengths.

Until the last two years, the detection rate of GRBs in the radio was around $\sim 30\%$. This small percentage (if compared to the optical and X-ray) remained unchanged before and after the launch of Swift (Chandra and Frail 2012). The ameliorated sensitivity of the upgraded Very Large Array (i.e. JVLA) increased the detection rate to 60% in the last two years. This seems to support the idea that the small detection rate was mainly due to the sensitivity limits of past radio follow up programs (Ghirlanda et al. 2013). Most often, these detections were at the level of sub-mJy flux densities in the 0.6–660 GHz (53% at 8.5 GHz) frequency range and were obtained within dedicated observing programmes with the largest radio telescopes (VLA, WSRT, ATCA, GMRT). The median peak luminosity of the detected long GRBs is 10^{31} erg s^{-1} Hz $^{-1}$ at 8.4GHz while the few detected short GRBs and SN/GRBs are a factor 100 and 10 less luminous, respectively. Regarding the distance scale of radio detected GRBs there seems to be no preference: both low redshift (e.g. GRB 980425 - Kulkarni et al. (1998)) and high redshift (GRB 090423 - Chandra et al. (2010)) events have been detected in the radio band.

In those events with multi epoch detections (i.e. radio light curve) a typical peak luminosity of $\sim 2 \times 10^{31}$ erg s^{-1} Hz $^{-1}$ is reached after about 10–20 days (3–6 days in the source rest frame) since the burst trigger. Typical post peak decay index is of order unity. Figure 14 shows the radio light curve (top panel) of GRB 030329, one of the GRBs with the densest/longest monitoring in the radio band so far. The light curve shows a peak at ~ 15 days at 8.5 GHz and slightly later (~ 45 days) at 5 GHz, a typical behaviour of the radio light curve. Within the standard afterglow model where the radiation is produced by synchrotron emission at the external shock (produced by the deceleration of the jet by the interstellar medium), the broad band spectral energy distribution (SED) can be described by a characteristic peak and at least three break frequencies: the self-absorption frequency ν_{sa} below which the spectrum is steep (with typical slopes $\nu^{2-5/2}$), the electron minimum frequency ν_m corresponding to the minimum energy (γ_m) of the relativistically shock accelerated electrons and the cooling frequency ν_c which corresponds to the minimum energy of the electrons that cool on dynamical timescales. The typical ordering is $\nu_{sa} < \nu_m <$

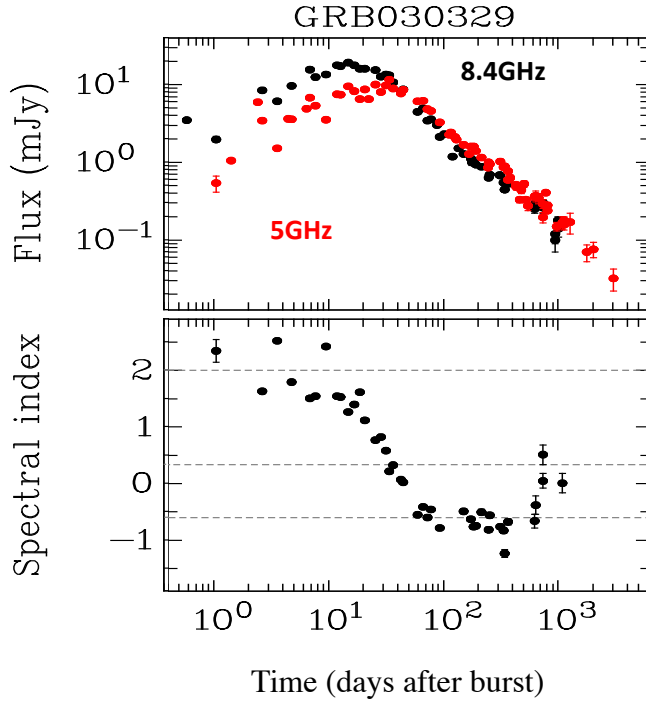


Fig. 14 Radio light curve (top panel) at 8.5GHz (black symbols) and 5GHz (red symbols) of GRB 030329. Evolution of the spectral index (computed between 5 and 8.5 GHz) as a function of time (bottom panel). Dashed lines in the bottom panel show reference slopes of $-2/3$, $1/3$ and 2 (from bottom to top). Figure adapted from Granot and van der Horst (2014).

ν_c at relatively early times (days–weeks) and $\nu_m < \nu_{sa} < \nu_c$ at late times. The evolution of these frequencies and of the peak flux with time depends on the jet dynamics. The standard afterglow model (e.g. van Eerten et al. (2012)) links the spectrum (dependent on the the micro physical parameters describing the shock - i.e. electron energy index, fraction of energy in relativistic electrons and in magnetic field) and the jet dynamics (dependent on the macro physical parameters, i.e. the kinetic energy of the jet and the density of the external medium).

The radio band, therefore, is affected by ν_{sa} and ν_m and their relative position. The appearance of a peak in the radio light curve is produced by the passage across the observing band of these frequencies. In the example of GRB 030329 shown in Figure 14 the bottom panel shows that the spectrum

is self absorbed at early times (with index -2 typical of the SED below ν_{sa}) and becomes softer at later times reaching a slope -0.6 which can be used to infer the electron energy power law slope, $p \sim 2.2$ in this case. The early time spectral variation is due to interstellar scintillation. In general, in the radio band, the time of the peak increases and its brightness decreases with decreasing radio frequency.

Radio emission, when detected, can be followed on very long timescales. While the X-ray (optical) afterglow fades below the sensitivity limits (below the host galaxy flux level) within weeks since the burst, radio emission has been observed years after (e.g. GRB 970508 - Frail et al. (2000); GRB 980703 - Mesler and Pihlström (2013)) with GRB 030329 (Figure 14) still detected at 5 GHz almost a decade after the γ -ray event. In this respect, radio observations are unique in probing the transition of the blast wave to the non-relativistic regime (i.e. trans-relativistic phase). In particular, during this phase estimates of the outflow parameters such as the kinetic energy (Frail et al. 2001; Berger et al. 2004; Frail et al. 2005; Shivvers and Berger 2011) do not depend on relativistic effects and jet aperture (if spherical symmetry is reached) differently from the same parameters estimates performed during the early relativistic phase (although radio calorimetry is not assumptions free - e.g. Eichler and Waxman (2005)).

Another unique feature of the radio band is the possibility to study the broad band SED of dark bursts (see e.g. Melandri et al. (2012) for a recent compilation of dark bursts properties): by combining multifrequency radio observations with X-ray data it is possible to model the time evolution of the SED and infer, for bursts without optical detection, an estimate of the optical extinction. One of the best cases, GRB 051022 (Rol et al. 2007), turned out to be highly extinguished (~ 2.3 mag in the infrared and at least 5.4 mag in the optical) possibly due to some dust clumps located along the line of sight within the host galaxy.

Polarisation is a powerful diagnostic of the jet composition. In particular, the reverse shock emission (produced by the deceleration shock propagating backwards into the jet outflow) and its polarisation level can constrain the magnetic field structure of the jet. Reverse shock emission in the optical band, characterized by a flare like light curve (i.e. with rise and decay steeper than the typical slopes predicted by the afterglow emission), has been observed in a handful of bursts (e.g. 080319B - Racusin et al. (2008); see Japelj et al. (2014)). Radio flares from the reverse shock has been observed only in a couple of bursts (990123 - Kulkarni et al. (1999)) with the most recent case of 130427A (Laskar et al. 2013). This is a relatively nearby GRB (at $z = 0.34$) with an extraordinary energetic budget (exceeding 10^{54} erg). Its emission has been detected up to the GeV band by Fermi and broadband SED modelling has produced different interpretations (e.g. Maselli et al. (2014)). The radio band offered the opportunity to interpret the early time radio flare as due to the reverse shock (also observed in the optical - Verstrand et al. 2013) suggesting a low density environment (Laskar et al. 2013; Perley et al. 2014). However, additional radio data (van der Horst et al. 2014) suggested also a possible

alternative interpretation of a double jet component. This bursts is one of the best examples where the combination of multi wavelength data allow us to break the degeneracy among the free parameters of the standard model while it still represents a challenge for the standard model itself (Maselli et al. 2014).

Radio afterglow observations offer in principle the unique opportunity to measure the jet expansion and constrain the GRB size. This can be done (i) directly through imaging as for (the only case) GRB 030329 which was observed to expand over a couple of months thus indicating an apparent velocity 3–5 the speed of light (Taylor et al. 2004; Pihlström et al. 2007; Mesler et al. 2012) or (ii) indirectly through radio scintillation (i.e. from the measurement of the time it is quenched when the projected source size is larger than the galactic ISM inhomogeneities causing it).

At very late times, when the afterglow emission has faded below the host galaxy, radio observations allows us to derive an independent estimate of the star formation in GRB hosts thus providing an estimate of the dust obscuration. Systematic search of radio host emission provided several upper limits at the level of 10–100 μJy and only few detections at redshift $z < 1$ (Michałowski et al. 2012; Perley and Perley 2013; Perley et al. 2015). Despite the small detection rates, these studies indicate that the host star formation rates derived from the radio, which have the advantage of probing the unobscured SFR are $\ll 100 M_{\odot} \text{ yr}^{-1}$. One major source of uncertainty in these estimates is the unknown host radio spectrum, which requires multifrequency observations. Radio hosts observations will shed light on the class of dark GRBs ($\sim 20\text{--}30$) i.e. bursts that are not detected in the Optical band (Perley et al. 2015).

6.2 The future of radio observations of GRBs

We are now entering the era of advanced radio facilities. The updated JVLA, the largest radio telescopes working in interferometric mode (VLBI, VLBA, EVN) and the advent of the SKA precursors are in the reach of detecting and monitoring GRBs. In particular, the Square Kilometer Array (SKA - Carilli et al. (2003)) will be the most powerful radio facility for continuum, spectroscopy and survey studies of the radio sky. The observatory will be composed of two sites (Australia and South Africa) where thousands of different antennas (from aperture arrays to single dishes) will be operated over a wide frequency range extending to 9 GHz at the highest frequencies.

Through a population synthesis code it is possible to predict the radio flux density at the time when the radio light curve peaks for a synthetic population of GRBs (Ghirlanda et al. 2013). The assumptions of this simulations are discussed in (Ghirlanda et al. 2013, 2014, 2015). Figure 15 shows the contour levels corresponding to the distribution of the simulated population. The axes represent the flux of the radio emission at the time when the peak of the emission is reached. The different contour levels refer to four characteristic frequencies of the SKA-MID configuration². The dashed lines are the 5σ

² <https://www.skatelescope.org/news/ska-science-book/>

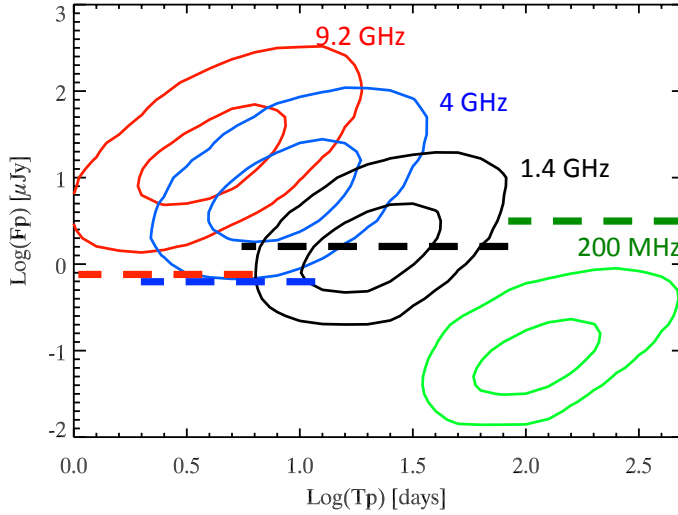


Fig. 15 Contour levels (68% and 95%) of the distribution of the population of GRBs corresponding to the time when the peak of the afterglow is reached and the corresponding flux. Four characteristic frequencies corresponding to the SKA1-MID (REF) are shown with different colors. The dashed lines show the expected continuum sensitivity limits at 5σ for a 12h exposure.

sensitivity limits obtained for a 12h exposure. Figure 15 shows that the characteristic timescale of the peak of the afterglow light curve moves to longer times at lower frequencies. Current estimates with the SKA1-MID sensitivity limits (Burlon et al. 2015) show that it will be possible to detect most of the population of GRBs at relatively large frequencies (from 4 to 9.2 GHz, blue and red curves in Figure 15). Still the self absorption dominating the lowest frequencies will make accessible with the SKA-1 roughly half of the bursts at 1.4GHz (black curves) and almost make it tough to detect any GRB at 200 MHz (green curves). These estimates only describe the power of the radio observations to study the radio afterglow emission of GRBs. In general the follow up campaigns of GRBs will strongly benefit from the increased sensitivities of present and forthcoming radio facilities provided that the detection rate of GRBs in the γ -ray band (i.e. the triggers) is maintained/increased with current/future GRB detectors (from Swift and Fermi now to SVOM in the future).

The high sensitivity of the SKA will make it possible to perform late time radio observations of the bursts when they have transitioned to the non-

relativistic regime. We have computed (Ghirlanda et al. 2013; Burlon et al. 2015) the expected flux density at the non-relativistic transition and compared to the SKA1-MID expected limits. Only a handful of objects reach the sensitivity limit of current facilities (a few μJy at best). We foresee that the full SKA will routinely observe a significant fraction (15–25%) of the whole GRB afterglow population at late times.

One challenging aspect of GRBs in the forthcoming era of extended radio facilities and in the final SKA era will be the possibility to access their parent population. We know that GRBs are jetted sources with a typical opening angle of a few degrees. We detect only those bursts whose jet is closely aligned with our line of sight. This means that for a burst that we detect in γ -rays there are hundreds of events that point their jet elsewhere. Depending on the jet structure these events can still be detected as slow transients in wide field surveys. Orphan afterglow properties have been studied in the literature Rossi et al. (2008); Ghirlanda et al. (2014, 2015). Despite their large number no convincing evidence of a radio orphan GRB has been reported so far. This is most likely due to the sensitivity limits of past radio surveys. Forthcoming radio surveys like the VAST/ASKAP (operating at 1.4 GHz) or the MeerKAT or EVLA (operating at 8.4 GHz) could detect 3×10^{-3} and 3×10^{-1} OA $\text{deg}^{-2} \text{yr}^{-1}$, respectively. The deeper SKA survey, reaching the μJy flux limit, could detect up to 0.2–1.5 OA $\text{deg}^{-2} \text{yr}^{-1}$ (Ghirlanda et al. 2014; Metzger et al. 2015).

The SKA era will be transformational for the study of GRBs. The SKA will access close to 100% of the GRBs detected in γ -rays and will substantially contribute to the multi-wavelength follow-up of these sources. Radio observations will extend the timescale of follow-up to very late times when the afterglow emission at other frequencies will be already undetectable. We will get an unprecedented insight into the true energy budget of GRBs and it will become possible to probe both the macrophysics of the ambient medium (e.g. the density profile) and the microphysics of the shocks. Finally, it will become possible to detect the so far elusive class of orphan afterglows that should appear as slowly evolving transients detectable with the SKA on a weekly basis in its wide field survey.

7 Lobster-eye micro-pore optics for X-ray focusing and the Einstein Probe mission

Time-domain astronomy will see its golden era towards the end of this decade with the advent of major wide-field facilities across the electromagnetic spectrum and in the multi-messenger realms including gravitational wave and neutrinos. In the X-ray regime, the driving science calls for new generation instruments with high sensitivity, good angular resolution (a few arc-minutes or less) and a large sky coverage (field of view of order of thousands square degrees). These requirements can be fulfilled by wide-field X-ray focusing optics—the emerging lobster-eye Micro-Pore Optics (MPO), as focusing imaging results in enormously enhanced gain in signal to noise, and thus high detecting sensitivity. The Einstein Probe (EP), which is a candidate mission of priority of the Chinese Academy of Sciences with an intended launch date around 2020, is based on this lobster-eye MPO technology. Its aim is to monitor a large fraction of the whole sky at high cadences with sensitivity in X-ray at least one order of magnitude deeper than the most sensitive all-sky monitoring type instruments ever built.

Among various types of faint transients that EP is expected to discover, high-redshift gamma-ray bursts are of particular interest since, as the most luminous objects in the Universe at their peaks, they provide a unique tool to study the early Universe beyond redshifts 6 and up to ~ 20 . During this epoch the first luminous objects as Pop-III stars (as well as Pop-II stars) are expected to form and start to re-ionise the Universe out of the dark ages (Ciardi and Ferrara 2005). Whilst synthesizing metals they quickly evolved and exploded, and thereby polluted their environment. The detection of these stars individually would be extremely difficult or almost impossible, however, even with the next generation of space observatories like JWST. The only way of observing Pop-III stars in action is to detect their explosive deaths. They have been predicted to produce a GRB-like event (Bromm and Loeb 2006; Wang et al. 2012). By using high-redshift GRBs as beacons we could identify and probe the regions where the first stars and their remnants (the first black holes) were formed.

7.1 Micro-pore optics X-ray focusing technology

X-ray focusing instruments rely on multiple smooth refraction surfaces almost parallel to incident X-rays, which can be arranged in several different configurations. One is Lobster-eye optics (Angel 1979), which mimics the imaging principle of the eyes of lobsters as shown in Figure 16. Incoming light is reflected off the walls of many tiny square pores arranged on a sphere and pointed towards the cocentric spherical center. The reflection surfaces are configured orthogonal to each other without a specific optical axis, and thus the FOV can in principle subtend the entire solid angle of 4π . In contrast, the conventional Wolter-I optics (Wolter 1952) (used for Chandra, XMM-Newton, Swift/XTR,

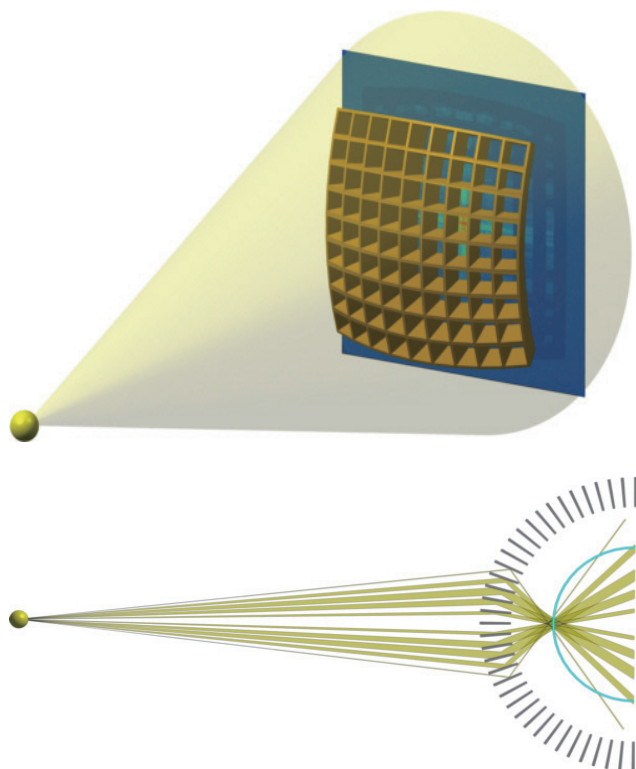


Fig. 16 Upper panel: Lobster eye optics: X-rays from source illuminate micro channel grid (gold colour) and are focused on detector plane with cross-like Pointing Spreading Function (right, blue). Lower panel: Optical path in a lobster eye optics. (Credit: adopted from <http://www.x-ray-optics.de/>).

etc.) has an tubular, rotationally symmetric elliptical or parabolic reflection surface followed by a hyperbolic surface, which is impossible to achieve a FOV larger than one degree.

Lobster-eye telescopes can be constructed using novel X-ray focusing device, the so-called Micro-Pore Optics (MPO) (Fraser et al. 1993). This technology integrates millions of square pores as shown in Figure 17 with sizes of about tens of micrometers on a very thin (~ 1 mm) glass piece of several square centimeters. The walls of pores are smooth enough to reflect X-ray photons up to several Kilo-eV. MPO is one of the most compact X-ray optics with the largest effective area to weight ratio. MPO is employed for the MIXS X-ray telescope onboard EAS's Mercury mission BepiColombo (Fraser et al. 2010), where a payload mass is strictly constrained, as well as for the MXT X-ray telescope onboard SVOM (Section 2). A lobster-eye telescope with MPO devices can achieve a huge instantaneous FOV with very light weight, which is unique for X-ray imaging telescopes.

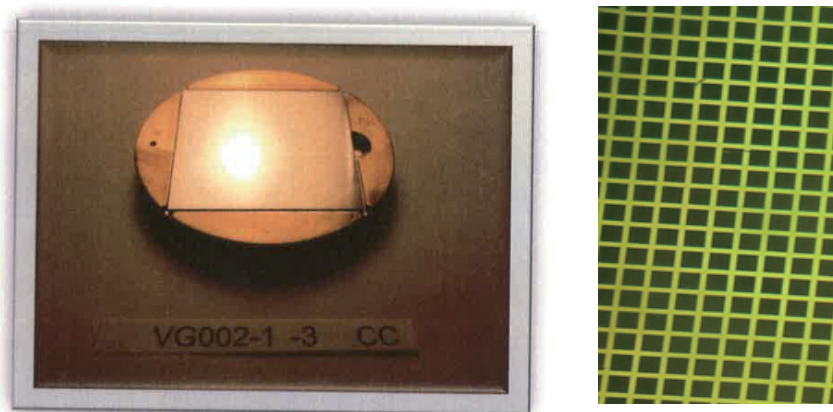


Fig. 17 MPO device (left) and a close-up under microscope (right). The pore size is of 20 micrometers.

A simulated point spread function (PSF) of a Lobster-eye telescope is shown in Figure 18. The cross-like feature is caused by complex reflection processes of X-ray photons across the square pore. The incoming X-rays are split into four beams corresponding respectively to no reflection (straight through, forming background), single reflection (cross arms) or double reflections off

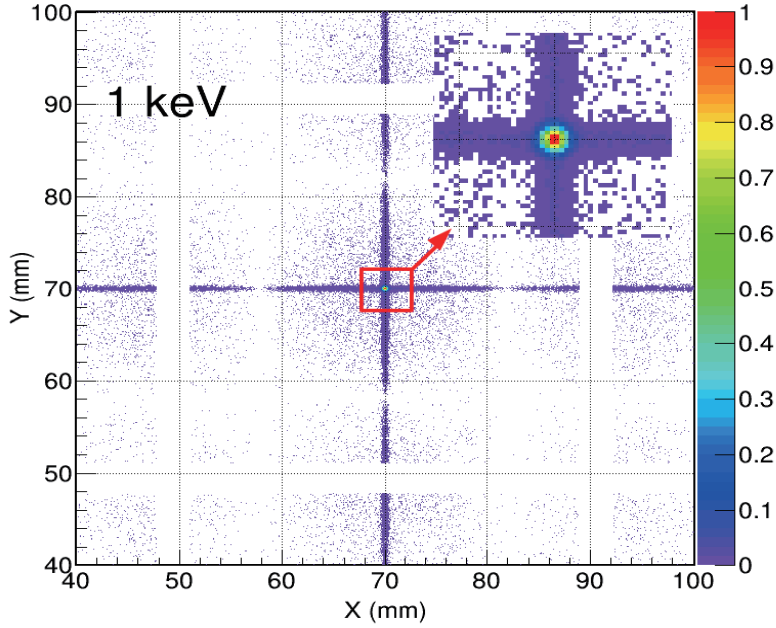


Fig. 18 Simulated PSF at 1 keV of a Lobster-eye telescope with a focal length of 375 mm.

adjacent walls of the pore (focal spot). The FoV of the optical arrangement indicated in Figure 16 is only limited by the size of the optics (the number of MPO pieces) or the size of the detector. The PSF remains almost unchanged over the entire FOV without vignetting of the effective area. Such a wide-field lobster-eye telescope provides the technological basis of the next generation wide-field X-ray monitors to detect faint and short-lived phenomena like high-redshift Gamma-Ray Bursts, distant X-ray novae and tidal disruption events.

7.2 Einstein Probe

The Einstein Probe is a candidate mission of priority in the Advanced Study Phase of the Space Science Pilot Programme of the Chinese Academy of Sciences (CAS), with an intended launch date around 2020. It will discover and characterise high-energy transients and monitor variable objects in the soft X-ray band with unprecedented sensitivity. Its primary scientific goals are to: (1) reveal quiescent black holes at almost all astrophysical mass scales and study how matter falls onto them by detecting transient X-ray flares, particularly stars being tidally-disrupted by otherwise dormant massive black holes at galactic centres; (2) discover the X-ray photonic counterparts of gravitational-wave transients found with the next generation of gravitational-wave detectors

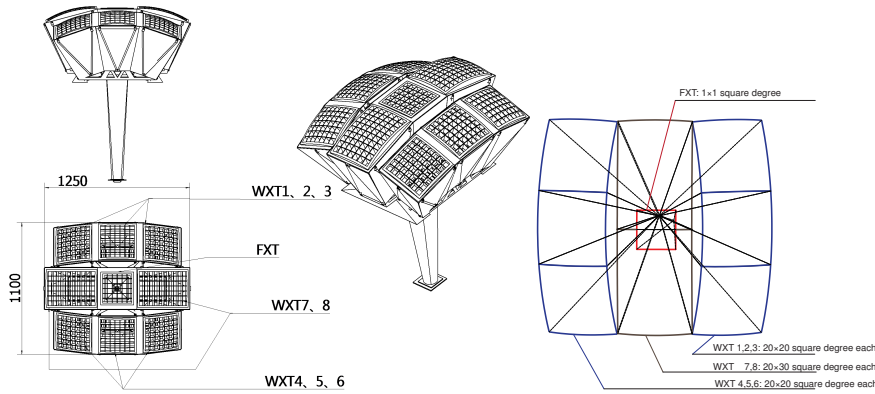


Fig. 19 (left) Layout of WXT modules and FXT. (right) Sketch of the field of view of WXT (not to scale). [Figures adopted from Yuan et al. (2015)].

and precisely locate them; (3) carry out systematic and sensitive surveys of high-energy transients, to discover faint X-ray transients of various types, such as high-redshift GRBs, supernova shock breakout, and previously unknown transients.

The payload of EP consists of a Wide-field X-ray Telescope (WXT) with a field-of-view of $60 \times 60 \text{ deg}^2$ in the nominal 0.5–4 keV band, and a Follow-up X-ray telescope (FXT) with a larger light-collecting power than WXT, both based on the lobster-eye MPO technology. In addition, EP is equipped with a fast alert telemetry system, in order to trigger multi-wavelength follow-up observations from the worldwide community. The nominal mission lifetime is three years with a goal of five years. For a more detailed description of the scientific goals and instrumentation of EP, please refer to Yuan et al. (2015).

The WXT telescope consists of eight modules, with FXT mounted at the center (Figure 19). Table 3 lists the main specifications of both WXT and FXT. The eight WXT modules make up a spherical array mosaicked by 441 concentric MPO pieces, each of 40mmx40mm in size. The total FoV subtends a solid angle of $60 \times 60 \text{ deg}^2$ (~ 1.1 steradian), which is about 1/11 of the whole sky. WXT has a large focal plane size, $420 \times 420 \text{ mm}^2$ in total. As a baseline detector, gas detectors based on GEM (Gas electron multiplier) are currently being developed. The effective area and sensitivity curve of WXT are shown in Figure 20. FXT is a narrow field-of-view ($\sim 1 \text{ deg}$) telescope of the same lobster-eye MPO type with a focal length of 1.4 m, yielding a much larger effective area ($\sim 80 \text{ cm}^2$ at 1 keV). FXT has an aperture size of about 240 mm, which is mosaicked by 6×6 MPO pieces. FXT will employ CCD as the focal plane detector to gain better spectral performance.

The layout of the EP satellite and its FoV as well as the observing mode are illustrated in Figure 21. The satellite will be in a circular orbit with an altitude of about 600 km and an inclination angle less than 30 degrees. The survey strategy of EP will be composed of a series of pointings (each of about

Table 3 Specifications of WXT and FXT

Parameters	WXT	FXT
Number of modules	8	1
Field-of-view	$60^\circ \times 60^\circ$	$1^\circ \times 1^\circ$
Focal length (mm)	375	1,400
Angular resolution FWHM (arcmin)	<5	<5
Nominal pandpass (keV)	0.5–4.0	0.5–4.0
Energy resolution @1 keV	40%	100 eV
Effective area (central focus + arms) (cm^2)	8 @0.7 keV	80 @1 keV
Sensitivity ($\text{erg s}^{-1} \text{cm}^{-2}$ @1,000 s)	$\sim 1 \times 10^{-11}$	$\sim 3 \times 10^{-12}$

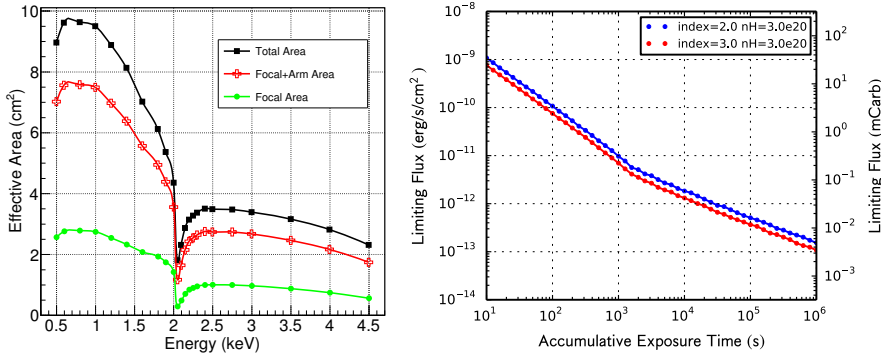


Fig. 20 (left) Simulated effective area of EP/WXT with a GEM detector, for the central focal spot (green), central plus the cruciform arms (red), and total (black; plus unfocused X-rays as diffuse background). The MPO arrays are coated with Iridium, and have surface roughness of ~ 0.55 nm and the tilts of pores following a Gaussian distribution with $\sigma=0.85$ arcmin. Xenon gas and a window of a 40 nm-thick Si_3N_4 foil coated with 30 nm-thick Aluminum are used for the detector. [Figure adopted from Zhao et al. (2014)]. (right) Detecting sensitivity as a function of accumulative exposure time (assuming a source spectrum of an absorbed power-law with a photon index of $\Gamma = 2$ and 3, respectively).

11-minute exposure) to mosaic the night sky in the directions avoiding the Sun. Over three orbits (~ 97 minutes each) almost the entire night sky will be sampled. The pointing directions are shifted by about 1 degree per day to compensate the daily movement of the Sun on the sky. In this way, the entire sky will be covered within half-a-year's operation. Once a transient source is detected with WXT and is classified and triggered by the processing and alerting system onboard, the satellite will slew to a new position to enable pointed follow-up observations of the new source with FXT. Meanwhile, WXT continues to monitor the new sky region centering the position of the transient. The alert data of transients are expected to be downlinked within one minute or so via the fast telemetry system, for which the French VHF system is considered.

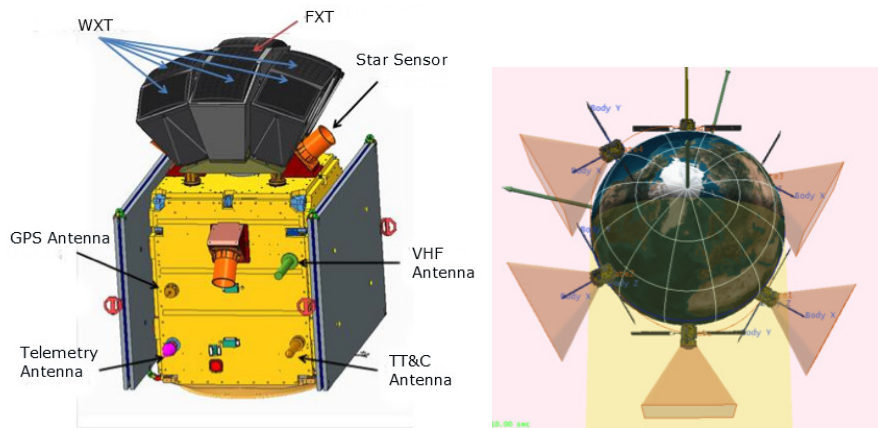


Fig. 21 (left) Layout of the Einstein Probe satellite. (right) Illustration of the field-of-view and pointed observations in one orbit. [Figures adopted from Yuan et al. (2015)].

7.3 Summary

The emerging lobster-eye MPO optics provides a promising technology to realise X-ray focusing, thus the improvement of detecting sensitivity, while retaining large field-of-view of over thousands of square degrees. Its application to X-ray all-sky monitors is expected to revolutionise the high-energy time-domain astrophysics. The Einstein Probe mission, which is based on this technology, will attempt to address some of the key questions in astrophysics and cosmology by capturing faint flashes of X-ray radiation produced by energetic events within a cosmic horizon far beyond the reach of any current and previous missions. Its scientific impact will span a wide range of research fields in astrophysics and fundamental physics, from stars, compact objects in our and nearby galaxies, black holes, supernovae, GRBs, galaxies to cosmology. In particular, EP has the capability of detecting high-redshift GRBs at $z \sim 10$ and beyond. It is expected that EP will detect 10 – 30 GRBs at $z > 6$ (3 – 9 GRBs at $z > 8$) per year (Wu et al., in preparation), and will thus deliver a considerable sample of high-redshift GRBs with which to study the early Universe within its nominal lifetime of three years.

8 THESEUS

8.1 Gamma-Ray Bursts as probes of the Early Universe

The study of the Universe before and during the epoch of reionization represents one of the major themes for the next generation of space and groundbased observational facilities. Many questions about the first phases of structure formation in the early Universe will still be open in the late 2020s: when and how did first stars/galaxies form? What are their properties? When and how fast was the Universe enriched with metals? How did reionization proceed?

Because of their huge luminosities, mostly emitted in the X and gamma-rays, their redshift distribution extending at least to $z \sim 10$ and their association with explosive death of massive stars and star forming regions, Gamma-Ray Bursts (GRBs) are unique and powerful tools for investigating the early Universe: SFR evolution, physics of re-ionization, galaxies metallicity evolution and luminosity function, first generation (pop III) stars.

The European community played a fundamental role in the enormous progress in the field of GRBs in the last 15–20 years (BeppoSAX, HETE-2, Swift, AGILE, Fermi, plus enormous efforts in optical IR and radio follow-up) In 2012, two European proposals for ESA Call for Small mission dedicated to GRBs and all-sky monitoring: GAME (led by Italy, SDD-based cameras + CZT-based camera + scintillator based detectors) and A-STAR (led by UK, lobster-eye telescopes + CdTe detectors). Following all this unique experience and efforts, a White Paper on GRBs as probes of the early Universe submitted in response to ESA Call for science theme for next L2/L3 missions (Amati et al. 2013) was very well considered by ESA.

The THESEUS proposal described below is a result and follow-on of all this unique experience and efforts by the European GRB community, reinforcing also the collaboration with extra-European (e.g., USA) GRB communities and opening itself to tight collaboration with the cosmology and transients astrophysical communities.

8.2 The THESEUS mission concept

The Transient High Energy Sky and Early Universe Surveyor (THESEUS) is a mission concept a mission concept that will be submitted to ESA in 2016 by a large international collaboration in response to the Call for next M5 mission within the Cosmic Vision Programme. The primary scientific goals of the mission are linked to the following Cosmic Vision themes: 4.1 Early Universe, 4.2 The Universe taking shape, and 4.3 The evolving violent Universe.

As detailed below, the main goal of THESEUS is fully exploiting GRBs as cosmological probes, thus providing a fundamental and unique step forward in our understanding of the early Universe. More in general, THESEUS would vastly increase the discovery space of several classes of high energy transient phenomena over the entire cosmic history.

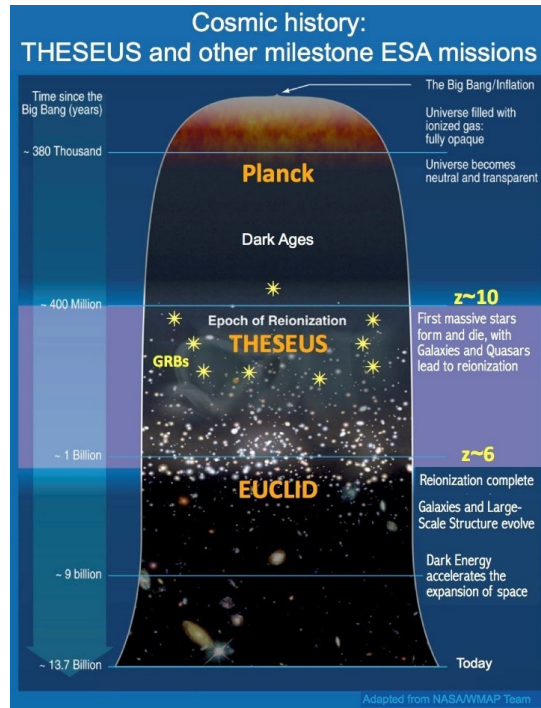


Fig. 22 Example of the complementarity and uniqueness of the THESEUS mission w/r to other cosmological measurements. (Credits: Caltech/NASA and the THESEUS Collaboration)

This is achieved via a unique payload providing an unprecedented combination of: (i) wide and deep sky monitoring in a broad energy band (0.3 keV–20 MeV); (ii) focusing capabilities in the soft X-ray band granting large grasp and high angular resolution; and 3) on board near-IR capabilities for immediate transient identification and first redshift estimate.

8.3 Scientific goals

The main scientific goals of THESUES can be summarized as follows.

(a) **Exploring the Early Universe (cosmic dawn and reionization era) by unveiling the Gamma-Ray Burst (GRBs) population in the first billion years**, namely to perform unprecedented studies of the star formation history up to $z \sim 8-9$ and more; to detect and study the primordial (pop III) star population: when did the first stars form and how did the earliest pop III and pop II stars influence their environments?; to investigate the re-ionization epoch, the interstellar medium (ISM) and intergalactic medium (IGM) up to $z \sim 8-9$ and more: how did re-ionization proceed as a function of

environment, and was radiation from massive stars its primary driver? How did cosmic chemical evolution proceed as a function of time and environment?; to investigate the properties of the early galaxies and what was the galaxies global star formation in the re-ionization era, and to investigate the dark energy properties and evolution. The complementarity of THESEUS under this respect with other “cosmology” mission investigating the CMB or the large scale structure of the Universe is illustrated in Figure 22.

(b) Performing an unprecedented deep survey of the soft X-ray transient Universe in order to: Fill the present gap in the discovery space of new classes of transients events, thus providing unexpected phenomena and discoveries; Provide a fundamental step forward in the comprehension of the physics of various classes of Galactic and extra-Galactic transients, like, e.g.: tidal disruption events TDE, magnetars /SGRs, SN shock break-out, Soft X-ray Transients SFXTS, thermonuclear bursts from accreting neutron stars, Novae, dwarf novae, stellar flares, AGNs / Blazars); Provide real time trigger and accurate (~ 1 arcmin within a few seconds; ~ 1 arcsec within a few minutes) location of (long/short) GRBs and high-energy transients for follow-up with next-generation optical (EELT), IR (JWT), radio (SKA), X-rays (ATHENA), TeV (CTA) or neutrino telescopes and identify electromagnetic counterpart of detections by next generation gravitational wave detectors.

Additional science. By satisfying the requirements coming from the above main science drivers, the THESEUS payload will also automatically be capable to perform excellent secondary and observatory science, e.g.: unprecedented insights in the physics and progenitors of GRBs and their connection with peculiar core-collapse SNe; substantially increased detection rate and characterization of subenergetic GRBs and X-Ray Flashes; IR survey and guest observer possibilities, thus allowing a strong community involvement; survey capabilities of transient phenomena similar to the Large Synoptic Survey Telescope (LSST) in the optical: a remarkable scientific synergy can be anticipated.

8.4 Payload and mission profile

The scientific goals which come from a full exploration of the early Universe requires the detection of a factor ten more GRBs (about 100) in the first billion years of the Universe ($z > 6$), in the 3 years prime mission life time of THESEUS. Such a requirement is well beyond the capabilities of current and near future GRB detectors (Swift/BAT, the most sensitive one, has detected only very few GRBs above $z = 6$ in 10 years). As supported by intensive simulations performed by us and other works in the literature, the needed substantial increase of high- z GRBs requires both an increase of ~ 1 order of magnitude in sensitivity and an extension of the detector passband down to the soft X-rays (0.5–1 keV). Such capabilities must be provided over a broad field of view (~ 1 sr) with a source location accuracy < 2 , in order to allow efficient counterpart detection, on-board spectroscopy and redshift measure-

Table 4 Main characteristics of the THESEUS/SXI instrument (Credits: P. O'Brien, J. Osborne, D. Willingale and the THESEUS Collaboration)

Energy band (keV)	0.3-5
Telescope type:	Lobster eye
Optics aperture (mm ²)	290x290
Optics configuration	7x7 square pore MCPs
MCP size (mm ²)	40x40
Focal length (mm)	300
Focal plane shape	spherical
Focal plane detectors	CCD array
Size of each CCD (mm ²)	61x61
Pixel size (μm)	30
Pixel Number	1024 x 1024
Number of CCDs	4
Field of View (square deg)	542.8
Angular accuracy (best, worst) (arcsec)	(<10, 105)

Table 5 Main characteristics of the THESEUS/XGS instrument (Credits: F. Fuschino, C. Labanti, M. Marisaldi and the THESEUS Collaboration)

Energy band (keV)	2-20000
Detection principle	Siswitch
Low-energy detector	Silicon Drift Detector
High energy detector	CsI(Tl)
Separation of energy losses in Si and CsI(Tl)	Pulse shape analysis
Number of modules	25
Size of each module (mm ³)	130x130x100
Lateral passive shielding/module	0.5 mm W
Slat collimator/module	0.5 mm W
Overall collimator FOV (FWHM)	1.8sr
Average useful area in the SXI FOV (cm ²)	~2000

ment and optical and IR follow-up observations. Such performances can best be obtained by including in the payload a monitor based on the lobster-eye telescope technique, capable of focusing soft X-rays in the 0.3–6 keV energy band over a large FOV. Such instrumentation has been under development for several years at the University of Leicester, has an high TRL level (e.g., BepiColombo) and can perform an all-sky survey in the soft X-rays with an unprecedented combination of FOV, source location accuracy (<1) and sensitivity thus addressing both main science goals of the mission. An onboard

Table 6 Main characteristics of the THESEUS/IRT instrument (Credits: A.J. Castro-Tirado, V. Reglero, D. Gotz and the THESEUS Collaboration)

Telescope type:	Cassegrain		
Primary & Secondary size:	700 mm & 230 mm		
Material:	SiC (for both optics and optical tube assembly)		
Detector type:	Teledyne Hawaii-2RG 2048 x 2048 pixels (18 μm each)		
Imaging plate scale	0".3/pixel		
Field of view:	10' x 10'	6' x 6'	2".1 x 2".1
Resolution ($\lambda/\Delta\lambda$):	2-3 (imaging)	20 (low-res)	1700 (high-res) with 0".4 slit
Sensitivity (AB mag):	H = 22.5 (30s)	H = 20.8 (300s)	H = 19.3 (1800s)
Filters:	ZYJH	Prism	VPH grating
Wavelength range (μm):	0.7-1.8 (imaging)	0.7-1.8 (low-res)	0.7-1.8 (high-res)
Total envelope size (mm):	800 \varnothing x 1800		
Power (W):	95		
Mass (kg):	112.6		

infrared telescope of the 0.5–1m class is also needed, together with spacecraft fast slewing capability (e.g., 30/min), in order to provide prompt identification of the GRB optical/IR counterpart, refinement of the position down to a few arcs (thus enabling follow-up with the largest ground and space observatories), on-board redshift determination and spectroscopy of the counterpart and of the host galaxy. The telescope may also be used for multiple observatory and survey science goals. Finally, the inclusion in the payload of a broad field of view hard X-ray detection system covering the same survey FOV as the lobster-eye telescopes and extending the energy band from few keV up to several MeV will increase significantly the capabilities of the mission. As the lobster-eye telescopes can be triggered by several classes of transient phenomena (e.g., flare stars, X-ray bursts, etc), the hard X-ray detection system provides an efficient means to identify true GRBs and detect other transient sources (e.g., short GRBs). The joint data from the three instruments will characterize transients in terms of luminosity, spectra and timing properties over a broad energy band, thus getting fundamental insights into their physics.

Based on the above, the THESEUS payload consists of the instruments shortly described below.

Soft X-ray Imager (SXI): a set of Lobster Eye (0.3–6 keV) telescopes covering a total FOV of 1 sr field with 0.5–1 arcmin source location accuracy. Each module is a focusing wide field lobster eye telescope based on the optical principles described in previous sections. The optics aperture is $290 \times 290 \text{ mm}^2$ formed by an array of 7×7 square pore Micro Channel Plates (MCPs). The MCPs are $40 \times 40 \text{ mm}^2$ and are mounted on a spherical frame with radius of curvature 600 mm (2 times the focal length of 300 mm). The open aperture provided by each plate is $38 \times 38 \text{ mm}^2$; the outer dimension of the optics frame is $320 \times 320 \text{ mm}^2$. The focal plane of each SXI module is a spherical surface

of radius of curvature 600 mm situated at a distance of 300 mm (the focal length) from the optics aperture. The detectors for each module comprise a 2×2 array of large format CCDs baselined to be supplied by e2v technologies (UK) Ltd. Each CCD has an active area of $61 \times 61 \text{ mm}^2$; the detectors are tilted to approximate to the spherical focal surface.

InfraRed Telescope (IRT): a 70 cm class near-infrared (up to 2 microns) telescope (IRT) with imaging and moderate spectral capabilities. The telescope (optics and tube assembly) will be made of SiC, a material that has been used in other space missions (such as Gaia, Herschel, Sentinel 2 and SPICA). Simulations using a 0.7 m aperture Cassegrain space borne NIR telescope (with a 0.23 m secondary mirror), using a Teledyne Hawaii-2RG 2048x2048 pixels detector (18 m/pixels, resulting in 0.3 arcsec/pix plate scale) show that, for a 22.5 (H) point like source in a single 300 s exposure one could expect a SNR of 6. In order to achieve such performances the telescope needs to be cooled at 240 (+/- 3) K by passive means, conductive and radiative insulations. Regarding the instrument, the optics box needs to be cooled to 190 (+/- 5) K to by a two stage cooler for which the first stage will cool the optics and the second stage (the cold end) will cool the IR detector itself to 95 (+/-10) K: this allows the detector dark current to be kept at an acceptable level. The mechanical envelope of IRT is a cylinder with 80 cm diameter and 180 cm height. A sun-shield is placed on top of the telescope baffle for IRT straylight protection. The thermal hardware is composed by a pulse tube cooling the Detector and FEE electronics and a set of thermal straps extracting the heat from the electronic boxes and camera optics coupled to a radiator located on the spacecraft structure. The overall telescope mass is 112.6 kg and the total power supply is 95W.

X-Gamma-rays Spectrometer (XGS): non-imaging spectrometer (XGS) based on SDD+CsI, covering the same FOV than the Lobster telescope extending its energy band up to 20 MeV. The XGS consists of 25 modules made of scintillator bars optically coupled to an array of Silicon Drift Detectors (SDD) PhotoDiodes (PD) tightly packaged to each other. Both SDD-PDs and scintillator detect X- and gamma-rays. The top SDD-PD, facing the X-/gamma-ray entrance window, is operated both as X-ray detector for low energy X-ray photons interacting in Silicon and as a read-out system of the scintillation light resulting from X-/gamma-ray interactions in the scintillator. The bottom SDD-PD at the other extreme of the crystal bar operates only as a read-out system for the scintillations. The discrimination between energy losses in Si and CsI is based on the different shape of charge pulses resulting from X-ray interactions in Si or from the collection of the scintillation light thanks to their different timing properties (Marisaldi et al. 2005). Each bar is made of scintillating crystal $5 \times 5 \times 30 \text{ mm}^3$ in size. Each extreme of the bar is covered with a PD for the read-out of the scintillation light, while the other sides of the bar are wrapped with a light reflecting material conveying the scintillation light towards the PDs. The scintillator material is CsI(Tl) peaking its light emission at about 560 nm. The PD is realized with the technique

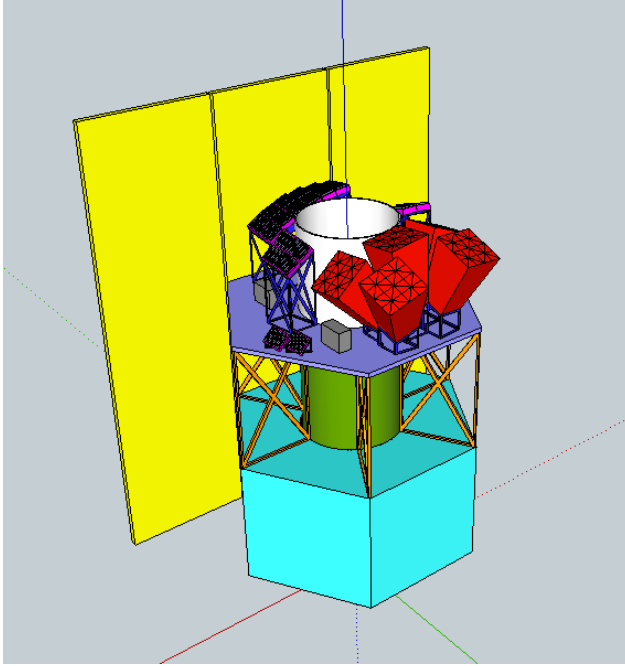


Fig. 23 Schematic view of the payload and satellite in THESEUS: the central green and white tube contains the IRT detectors, optics and baffle; the red modules are the SXI; the black-pink modules are the XGS. (Credits: F. Fuschino, C. Labanti and the THESEUS Collaboration)

of Silicon Drift Detectors with an active area of $5 \times 5 \text{ mm}^2$ so matching the scintillator cross section.

The main instruments characteristics are summarized in Tables 4, 5 and 6, and a possible payload accommodation sketch is shown in Figure 23. Sensitivity curves of the SXI and XGS are jointly shown in Figure 24. Examples of expected performances in terms of GRB detection rate as a function of redshift and rate of different classes of transients are shown in Figure 25 and Table 7, respectively.

8.5 Mission profile and consortium

The proposed mission profile includes an onboard data handling (OBDR) system capable of detecting, identifying and localizing likely transients in the SXI and XGS FOV; the capability of promptly (within a few tens of seconds at most) transmitting to ground the trigger time and position of GRBs (and other transients of interest); and a spacecraft slewing capability of $30^\circ/\text{min}$. The baseline launcher / orbit configuration is a launch with Vega to a low inclination low Earth orbit (LEO, $\sim 600 \text{ km}$, $< 5^\circ$), which has the unique advantages of granting a low and stable background level in the high-energy instruments,

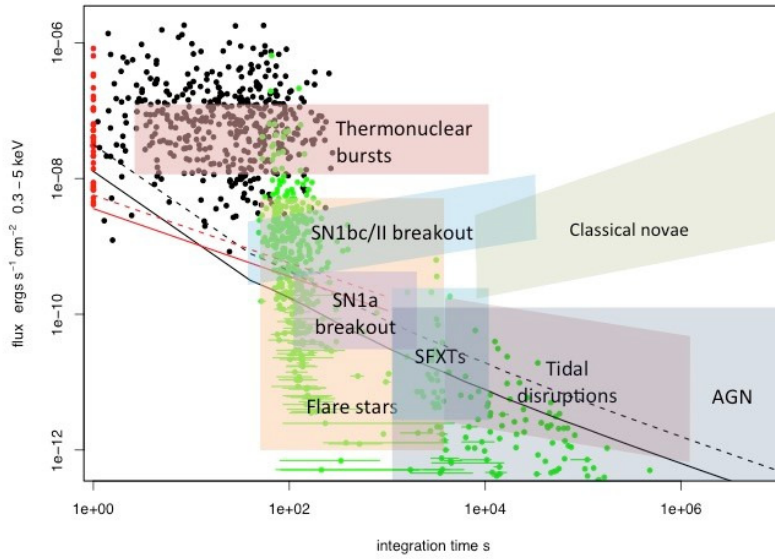


Fig. 24 Sensitivity of the SXI (black curves) and XGS (red) vs. integration time. The solid curves assume a source column density of $5 \times 10^{20} \text{ cm}^{-2}$ (i.e. well out of the Galactic plane and very little intrinsic absorption). The dotted curves assume a source column density of 10^{22} cm^{-2} (significant intrinsic absorption). The black dots are the peak fluxes for Swift BAT GRBs plotted against $T_{90}/2$. The flux in the soft band 0.3–10 keV was estimated using the T90 BAT spectral fit including the absorption from the XRT spectral fit. The red dots are those GRBs for which $T_{90}/2$ is less than 1 second. The green dots are the initial fluxes and times since trigger at the start of the Swift XRT GRB light-curves. The horizontal lines indicate the duration of the first time bin in the XRT light-curve. The various shaded regions illustrate variability and flux regions for different types of transients and variable sources. (Credits: D. Willingale, P. O’Brien, J. Osborne and the THESEUS Collaboration)

allowing the exploitation of the Earth’s magnetic field for spacecraft fast slewing and facilitating the prompt transmission of transients trigger and positions to ground. The basic observing strategy ASI antenna in Malindi and, as an option, the Brazilian antenna in Alcantara were proposed as ground stations. The basic observing strategy is based on alternating anti-sun and \sim polar pointing, a compromise between maximum sky coverage, optimization of follow-up observations from the ground, instruments requirements (thermal, etc.). Considered prompt downlink options include: NASA/TDRSS, ESA/EDRS, WHF network, IRIDIUM network, ORBCOMM. MOC and SOC were proposed to be managed by ESA, while the SDC was proposed to be managed by ASI (ASDC).

The total payload mass of THESEUS, including all contingencies, was estimated to be ~ 350 kg, and the total spacecraft dry mass about 1000 kg (power about 230 W and 800 W, respectively). The foreseen telemetry budget is fully

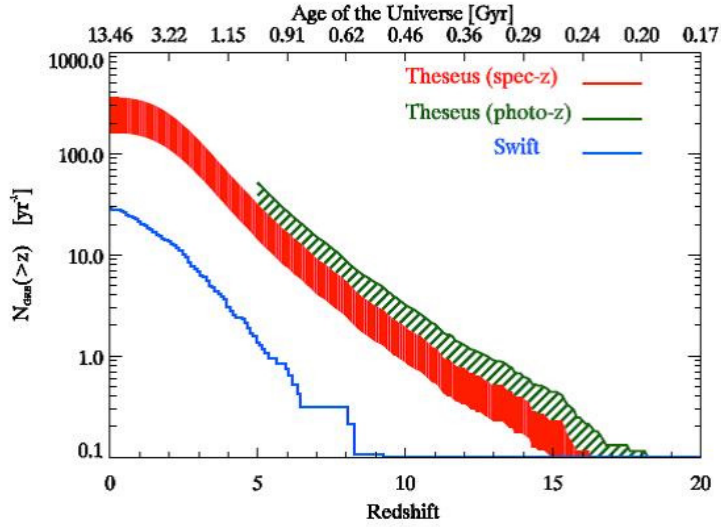


Fig. 25 The annual rate of GRBs predicted for THESEUS SXI (red) compared to Swift (blue). The upper scale shows the age of the Universe. For Swift the actual number of known redshifts is approximately one third that plotted and none were determined on board (the blue curve has been linearly scaled upwards to match the total Swift trigger rate). For THESEUS the red region uses the simulations from Ghirlanda et al. (2015) and adopts the instrument sensitivity for the SXI. (Credits: G. Ghirlanda, R. Salvaterra and the THESEUS Collaboration)

Table 7 Theseus detection rates for different astrophysical transients and variables (Credits: J. Osborne, P. O’Brien, D. Willingale and the THESEUS Collaboration)

Transient type	SXI Rate
GW sources	0.03-33 yr ⁻¹
Magnetars	40 day ⁻¹
SN shock breakout	4 yr ⁻¹
TDE	50 yr ⁻¹
AGN+Blazars	350 day ⁻¹
Thermonuclear bursts	35 day ⁻¹
Novae	250 yr ⁻¹
Dwarf novae	30 day ⁻¹
SFXTs	1000 yr ⁻¹
Stellar flares	400 yr ⁻¹
Stellar super flares	200 yr ⁻¹

compatible with the capabilities of the X-band, which will be the standard for next ESA M missions.

The THESEUS payload consortium for the ESA/M4 proposal is organized as follow. The SXI will be responsibility of the UK (led by the University of Leicester), the XGS will be responsibility of Italy (led by INAF, the University of Ferrara and INFN), and the IRT will be the responsibility of Spain (a consortium led by IAA-CSIC including UV, INTA, UGR and UMA) for the camera and ESA for the optics. The core consortium includes also Poland (led by CBK) and Denmark (led by DTU) for payload data handling hardware and software. Czech Republic (led by CTU) is also involved for contributions to the SXI, as well as Slovenia (SPACE-SI) for communications. France (CNES, CEA) is available to provide the SVOM network of VHF antennae and associated control center. A junior international contribution is foreseen by USA (NASA) for the TDRSS system and contributions to the XGS and IRT camera. Finally, Hungary and Ireland have declared its interest in investigating their contributions to different payload components during assessment phase.

Acknowledgements The authors are grateful to the International Space Science Institute of Beijing (ISSI-Beijing), its executive director Prof. M. Falanga and all the staff for hosting and funding the workshop “Gamma-Ray Bursts: a tool to Explore the Young Universe” held in Beijing from April 10 to 15 2015. W. Yuan and C. Zhang thank R. Willingale, J.P. Osborne and P. O’Brien for their contribution to the EP project and acknowledge support of the “Strategic Priority Research Program on Space Science” (Grant number No. XDA04061100) of the Chinese Academy of Sciences. B. Cordier and D. Götz acknowledge financial support of the UnivEarthS Labex program at Sorbonne Paris Cité (ANR-10-LABX-0023 and ANR-11-IDEX-0005-02). Sun acknowledges support from the 973 program 2014CB845802 and NSFC 11503028.

References

- C.W. Akerlof, H.F. Swan, An Estimation of the Gamma-Ray Burst Afterglow Apparent Optical Brightness Distribution Function. *ApJ* **671**, 1868–1876 (2007). doi:10.1086/523081
- L. Amati, J.-L. Atteia, L. Balazs, S. Basa, J. Becker Tjus, D.F. Bersier, M. Boer, S. Campana, B. Ciardi, S. Covino, F. Daigne, M. Feroci, A. Ferrara, F. Frontera, J.P.U. Fynbo, G. Ghirlanda, G. Ghisellini, S. Glover, J. Greiner, D. Gotz, L. Hanlon, J. Hjorth, R. Hudec, U. Katz, S. Khochfar, R. Klessen, M. Kowalski, A.J. Levan, S. McBreen, A. Mesinger, R. Mochkovitch, P. O’Brien, J.P. Osborne, P. Petitjean, O. Reimer, E. Resconi, S. Rosswog, F. Ryde, R. Salvaterra, S. Savaglio, R. Schneider, G. Tagliaferri, N.R. Tanvir, A. van der Horst, Light from the Cosmic Frontier: Gamma-Ray Bursts. *ArXiv e-prints* (2013)
- J.R.P. Angel, Lobster eyes as X-ray telescopes. *ApJ* **233**, 364–373 (1979). doi:10.1086/157397
- D. Band, J. Matteson, L. Ford, B. Schaefer, D. Palmer, B. Teegarden, T. Cline, M. Briggs, W. Paciesas, G. Pendleton, G. Fishman, C. Kouveliotou, C. Meegan, R. Wilson, P. Lestrade, BATSE observations of gamma-ray burst spectra. I - Spectral diversity. *ApJ* **413**, 281–292 (1993). doi:10.1086/172995
- E. Berger, S.R. Kulkarni, D.A. Frail, The Nonrelativistic Evolution of GRBs 980703 and 970508: Beaming-independent Calorimetry. *ApJ* **612**, 966–973 (2004). doi:10.1086/422809
- V. Bromm, A. Loeb, High-Redshift Gamma-Ray Bursts from Population III Progenitors. *ApJ* **642**, 382–388 (2006). doi:10.1086/500799
- D. Burlon, G. Ghirlanda, A. van der Horst, T. Murphy, R.A.M.J. Wijers, B. Gaensler, G. Ghisellini, I. Prandoni, The SKA View of Gamma-Ray Bursts. *Advancing Astrophysics with the Square Kilometre Array (AASKA14)*, 52 (2015)
- S. Campana, R. Salvaterra, A. Melandri, S.D. Vergani, S. Covino, P. D’Avanzo, D. Fugazza, G. Ghisellini, B. Sbarufatti, G. Tagliaferri, The X-ray absorbing column density of a complete sample of bright Swift gamma-ray bursts. *MNRAS* **421**, 1697–1702 (2012)
- C.L. Carilli, R.J. Ivison, D.A. Frail, Variability of Submillijansky Radio Sources. *ApJ* **590**, 192–196 (2003)
- P. Chandra, D.A. Frail, A Radio-selected Sample of Gamma-Ray Burst Afterglows. *ApJ* **746**, 156 (2012). doi:10.1088/0004-637X/746/2/156
- P. Chandra, D.A. Frail, D. Fox, S. Kulkarni, E. Berger, S.B. Cenko, D.C.-J. Bock, F. Harrison, M. Kasliwal, Discovery of Radio Afterglow from the Most Distant Cosmic Explosion. *ApJL* **712**, 31–35 (2010). doi:10.1088/2041-8205/712/1/L31
- H.-W. Chen, J.X. Prochaska, E. Ramirez-Ruiz, J.S. Bloom, M. Dessauges-Zavadsky, R.J. Foley, On the Absence of Wind Signatures in GRB Afterglow Spectra: Constraints on the Wolf-Rayet Winds of GRB Progenitors. *ApJ* **663**, 420–436 (2007). doi:10.1086/518111
- R. Chornock, E. Berger, D.B. Fox, R. Lunnan, M.R. Drout, W.-f. Fong, T. Laskar, K.C. Roth, GRB 130606A as a Probe of the Intergalactic Medium and the Interstellar Medium in a Star-forming Galaxy in the First Gyr after the Big Bang. *ApJ* **774**, 26 (2013). doi:10.1088/0004-637X/774/1/26
- B. Ciardi, A. Ferrara, The First Cosmic Structures and Their Effects. *Space Sci. Rev.* **116**, 625–705 (2005). doi:10.1007/s11214-005-3592-0

- B. Cordier, F. Desclaux, J. Foliard, S. Schanne, SVOM pointing strategy: how to optimize the redshift measurements?, in *American Institute of Physics Conference Series*, ed. by M. Galassi, D. Palmer, E. Fenimore American Institute of Physics Conference Series, vol. 1000, 2008, pp. 585–588. doi:10.1063/1.2943538
- E. Costa, F. Frontera, J. Heise, M. Feroci, J. in't Zand, F. Fiore, M.N. Cinti, D. Dal Fiume, Nicastro, Discovery of an X-ray afterglow associated with the γ -ray burst of 28 February 1997. *Nature* **387**, 783–785 (1997)
- A. Cucchiara, A.J. Levan, D.B. Fox, N.R. Tanvir, T.N. Ukwatta, E. Berger, T. Krühler, A. Küpcü Yoldaş, X.F. Wu, K. Toma, J. Greiner, F.E. Olivares, A. Rowlinson, L. Amati, T. Sakamoto, K. Roth, A. Stephens, A. Fritz, J.P.U. Fynbo, J. Hjorth, D. Malesani, P. Jakobsson, K. Wiersema, P.T. O'Brien, A.M. Soderberg, R.J. Foley, A.S. Fruchter, J. Rhoads, R.E. Rutledge, B.P. Schmidt, M.A. Dopita, P. Podsiadlowski, R. Willingale, C. Wolf, S.R. Kulkarni, P. D'Avanzo, A Photometric Redshift of $z \sim 9.4$ for GRB 090429B. *ApJ* **736**, 7 (2011). doi:10.1088/0004-637X/736/1/7
- E. Curtis-Lake, R.J. McLure, J.S. Dunlop, A.B. Rogers, T. Targett, A. Dekel, R.S. Ellis, S.M. Faber, H.C. Ferguson, N.A. Grogin, K.-H. Huang, D.D. Kocevski, A.M. Koekemoer, K. Lai, E. Mármol-Queraltó, B.E. Robertson, No evidence for evolution in the typical rest-frame UV sizes or the incidence of morphological disturbance amongst L_* galaxies at $4 < z < 8$. ArXiv e-prints (2014)
- D. Eichler, E. Waxman, The Efficiency of Electron Acceleration in Collisionless Shocks and Gamma-Ray Burst Energetics. *ApJ* **627**, 861–867 (2005). doi:10.1086/430596
- D.A. Frail, E. Waxman, S.R. Kulkarni, A 450 Day Light Curve of the Radio Afterglow of GRB 970508: Fireball Calorimetry. *ApJ* **537**, 191–204 (2000). doi:10.1086/309024
- D.A. Frail, S.R. Kulkarni, R. Sari, S.G. Djorgovski, J.S. Bloom, T.J. Galama, D.E. Reichart, E. Berger, F.A. Harrison, P.A. Price, S.A. Yost, A. Diercks, R.W. Goodrich, F. Chaffee, Beaming in Gamma-Ray Bursts: Evidence for a Standard Energy Reservoir. *ApJL* **562**, 55–58 (2001)
- D.A. Frail, A.M. Soderberg, S.R. Kulkarni, E. Berger, S. Yost, D.W. Fox, F.A. Harrison, Accurate Calorimetry of GRB 030329. *ApJ* **619**, 994–998 (2005). doi:10.1086/426680
- G.W. Fraser, A.N. Brunton, J.E. Lees, J.F. Pearson, W.B. Feller, X-ray focusing using square-pore microchannel plates First observation of cruxiform image structure. *Nuclear Instruments and Methods in Physics Research A* **324**, 404–407 (1993). doi:10.1016/0168-9002(93)91003-6
- G.W. Fraser, J.D. Carpenter, D.A. Rothery, J.F. Pearson, A. Martindale, J. Huovelin, J. Treis, M. Anand, M. Anttila, M. Ashcroft, J. Benkoff, P. Bland, A. Bowyer, A. Bradley, J. Bridges, C. Brown, C. Bulloch, E.J. Bunce, U. Christensen, M. Evans, R. Fairbend, M. Feasey, F. Giannini, S. Hermann, M. Hesse, M. Hilchenbach, T. Jordan, K. Joy, M. Kaipiainen, I. Kitchingman, P. Lechner, G. Lutz, A. Malkki, K. Muinonen, J. Näränen, P. Portin, M. Prydderch, J.S. Juan, E. Sclater, E. Schyns, T.J. Stevenson, L. Strüder, M. Syrjasuo, D. Talboys, P. Thomas, C. Whitford, S. Whitehead, The mercury imaging x-ray spectrometer (mixs) on bepicolombo. *Planetary and Space Science* **58**(1–2), 79–95 (2010). Comprehensive Science Investigations of Mercury: The scientific goals of the joint ESA/JAXA mission BepiColombo. doi:http://dx.doi.org/10.1016/j.pss.2009.05.004. http://www.sciencedirect.com/science/article/pii/S0032063309001482
- J.P.U. Fynbo, P. Jakobsson, J.X. Prochaska, D. Malesani, C. Ledoux, A. de Ugarte Postigo, M. Nardini, P.M. Vreeswijk, K. Wiersema, J. Hjorth, J. Sollerman, H.-W. Chen, C.C. Thöne, G. Björnsson, J.S. Bloom, A.J. Castro-Tirado, L. Christensen, A. De Cia, A.S. Fruchter, J. Gorosabel, J.F. Graham, A.O. Jaunsen, B.L. Jensen, D.A. Kann, C. Kouveliotou, A.J. Levan, J. Maund, N. Masetti, B. Milvang-Jensen, E. Palazzi, D.A. Perley, E. Pian, E. Rol, P. Schady, R.L.C. Starling, N.R. Tanvir, D.J. Watson, D. Xu, T. Augusteijn, F. Grundahl, J. Telting, P.-O. Quirion, Low-resolution Spectroscopy of Gamma-ray Burst Optical Afterglows: Biases in the Swift Sample and Characterization of the Absorbers. *ApJS* **185**, 526–573 (2009). doi:10.1088/0067-0049/185/2/526
- N. Gehrels, E. Ramirez-Ruiz, D.B. Fox, Gamma-Ray Bursts in the Swift Era. *ARA&A* **47**, 567–617 (2009). doi:10.1146/annurev.astro.46.060407.145147
- B. Gendre, G. Stratta, J.L. Atteia, S. Basa, M. Boër, D.M. Coward, S. Cutini, V. D'Elia, E.J. Howell, A. Klotz, L. Piro, The Ultra-long Gamma-Ray Burst 111209A: The Collapse of a Blue Supergiant? *ApJ* **766**, 30 (2013). doi:10.1088/0004-637X/766/1/30

- G. Ghirlanda, R. Salvaterra, D. Burlon, S. Campana, A. Melandri, M.G. Bernardini, S. Covino, P. D'Avanzo, V. D'Elia, G. Ghisellini, L. Nava, I. Prandoni, L. Sironi, G. Tagliaferri, S.D. Vergani, A. Wolter, Radio afterglows of a complete sample of bright Swift GRBs: predictions from present days to the SKA era. *MNRAS* **435**, 2543–2551 (2013)
- G. Ghirlanda, D. Burlon, G. Ghisellini, R. Salvaterra, M.G. Bernardini, S. Campana, S. Covino, P. D'Avanzo, V. D'Elia, A. Melandri, T. Murphy, L. Nava, S.D. Vergani, G. Tagliaferri, GRB Orphan Afterglows in Present and Future Radio Transient Surveys. *PASA* **31**, 22 (2014)
- G. Ghirlanda, R. Salvaterra, S. Campana, S.D. Vergani, J. Japelj, M.G. Bernardini, D. Burlon, P. D'Avanzo, A. Melandri, A. Gomboc, F. Nappo, R. Paladini, A. Pescalli, O.S. Salafia, G. Tagliaferri, Unveiling the population of orphan γ -ray bursts. *A&A* **578**, 71 (2015). doi:10.1051/0004-6361/201526112
- R. Gilmozzi, J. Spyromilio, The European Extremely Large Telescope (E-ELT). *The Messenger* **127**, 11 (2007)
- O. Godet, G. Nasser, J.-. Atteia, B. Cordier, P. Mandrou, D. Barret, H. Triou, R. Pons, C. Amoros, S. Bordon, O. Gevin, F. Gonzalez, D. Götz, A. Gros, B. Houret, C. Lachaud, K. Lacombe, W. Marty, K. Mercier, D. Rambaud, P. Ramon, G. Rouaix, S. Schanne, V. Waeghebaert, The x-/gamma-ray camera ECLAIRS for the gamma-ray burst mission SVOM, in *Society of Photo-Optical Instrumentation Engineers (SPIE) Conference Series*. Society of Photo-Optical Instrumentation Engineers (SPIE) Conference Series, vol. 9144, 2014, p. 24. doi:10.1117/12.2055507
- D. Götz, J. Osborne, B. Cordier, J. Paul, P. Evans, A. Beardmore, A. Martindale, R. Willingale, P. O'Brien, S. Basa, C. Rossin, O. Godet, N. Webb, J. Greiner, K. Nandra, N. Meidinger, E. Perinati, A. Santangelo, K. Mercier, F. Gonzalez, The microchannel x-ray telescope for the gamma-ray burst mission SVOM, in *Society of Photo-Optical Instrumentation Engineers (SPIE) Conference Series*. Society of Photo-Optical Instrumentation Engineers (SPIE) Conference Series, vol. 9144, 2014, p. 23. doi:10.1117/12.2054898
- J. Granot, A.J. van der Horst, Gamma-Ray Burst Jets and their Radio Observations. *PASA* **31**, 8 (2014). doi:10.1017/pasa.2013.44
- J. Greiner, W. Bornemann, C. Clemens, M. Deuter, G. Hasinger, M. Honsberg, H. Huber, S. Huber, M. Krauss, T. Krühler, A. Küpcü Yoldaş, H. Mayer-Hasselwander, B. Mican, N. Primak, F. Schrey, I. Steiner, G. Szokoly, C.C. Thöne, A. Yoldaş, S. Klose, U. Laux, J. Winkler, GROND—a 7-Channel Imager. *PASP* **120**, 405–424 (2008). doi:10.1086/587032
- O.E. Hartoog, D. Malesani, J.P.U. Fynbo, T. Goto, T. Krühler, P.M. Vreeswijk, A. De Cia, D. Xu, P. Møller, S. Covino, V. D'Elia, H. Flores, P. Goldoni, J. Hjorth, P. Jakobsson, J.-K. Krogager, L. Kaper, C. Ledoux, A.J. Levan, B. Milvang-Jensen, J. Sollerman, M. Sparre, G. Tagliaferri, N.R. Tanvir, A. de Ugarte Postigo, S.D. Vergani, K. Wiersema, J. Datson, R. Salinas, K. Mikkelsen, N. Aghanim, VLT/X-Shooter spectroscopy of the afterglow of the Swift GRB 130606A. Chemical abundances and reionisation at $z \sim 6$. *A&A* **580**, 139 (2015). doi:10.1051/0004-6361/201425001
- A. Heger, C.L. Fryer, S.E. Woosley, N. Langer, D.H. Hartmann, How Massive Single Stars End Their Life. *ApJ* **591**, 288–300 (2003). doi:10.1086/375341
- J. Heise, J.I. Zand, R.M. Kippen, P.M. Woods, X-Ray Flashes and X-Ray Rich Gamma Ray Bursts, in *Gamma-ray Bursts in the Afterglow Era*, ed. by E. Costa, F. Frontera, J. Hjorth, 2001, p. 16. doi:10.1007/10853853_4
- J. Japelj, D. Kopač, S. Kobayashi, R. Harrison, C. Guidorzi, F.J. Virgili, C.G. Mundell, A. Melandri, A. Gomboc, Phenomenology of Reverse-shock Emission in the Optical Afterglows of Gamma-Ray Bursts. *ApJ* **785**, 84 (2014). doi:10.1088/0004-637X/785/2/84
- A. Klotz, M. Boër, J.L. Atteia, B. Gendre, Early Optical Observations of Gamma-Ray Bursts by the TAROT Telescopes: Period 2001–2008. *AJ* **137**, 4100–4108 (2009). doi:10.1088/0004-6256/137/5/4100
- S.R. Kulkarni, D.A. Frail, M.H. Wieringa, R.D. Ekers, E.M. Sadler, R.M. Wark, J.L. Higdon, E.S. Phinney, J.S. Bloom, Radio emission from the unusual supernova 1998bw and its association with the γ -ray burst of 25 April 1998. *Nature* **395**, 663–669 (1998). doi:10.1038/27139
- S.R. Kulkarni, D.A. Frail, R. Sari, G.H. Moriarty-Schieven, D.S. Shepherd, P. Udomprasert, A.C.S. Readhead, J.S. Bloom, M. Feroci, E. Costa, Discovery of a Radio Flare from

- GRB 990123. *ApJL* **522**, 97–100 (1999). doi:10.1086/312227
- P. Kumar, B. Zhang, The physics of gamma-ray bursts and relativistic jets. *Physics Rep.* **561**, 1–109 (2015). doi:10.1016/j.physrep.2014.09.008
- D.Q. Lamb, D.E. Reichart, Gamma-Ray Bursts as a Probe of the Very High Redshift Universe. *ApJ* **536**, 1–18 (2000). doi:10.1086/308918
- T. Laskar, E. Berger, B.A. Zauderer, R. Margutti, A.M. Soderberg, S. Chakraborti, R. Lunnan, R. Chornock, P. Chandra, A. Ray, A Reverse Shock in GRB 130427A. *ApJ* **776**, 119 (2013). doi:10.1088/0004-637X/776/2/119
- A. Maselli, A. Melandri, L. Nava, C.G. Mundell, N. Kawai, S. Campana, S. Covino, J.R. Cummings, G. Cusumano, P.A. Evans, G. Ghirlanda, G. Ghisellini, C. Guidorzi, S. Kobayashi, P. Kuin, V. La Parola, V. Mangano, S. Oates, T. Sakamoto, M. Serino, F. Virgili, B.-B. Zhang, S. Barthelmy, A. Beardmore, M.G. Bernardini, D. Bersier, D. Burrows, G. Calderone, M. Capalbi, J. Chiang, P. D’Avanzo, V. D’Elia, M. De Pasquale, D. Fugazza, N. Gehrels, A. Gomboc, R. Harrison, H. Hanayama, J. Japelj, J. Kennea, D. Kopac, C. Kouveliotou, D. Kuroda, A. Levan, D. Malesani, F. Marshall, J. Nousek, P. O’Brien, J.P. Osborne, C. Pagani, K.L. Page, M. Perri, T. Pritchard, P. Romano, Y. Saito, B. Sbarufatti, R. Salvaterra, I. Steele, N. Tanvir, G. Vianello, B. Weigand, K. Wiersema, Y. Yatsu, T. Yoshii, G. Tagliaferri, GRB 130427A: A Nearby Ordinary Monster. *Science* **343**, 48–51 (2014). doi:10.1126/science.1242279
- M. McQuinn, A. Lidz, M. Zaldarriaga, L. Hernquist, S. Dutta, Probing the neutral fraction of the IGM with GRBs during the epoch of reionization. *MNRAS* **388**, 1101–1110 (2008). doi:10.1111/j.1365-2966.2008.13271.x
- N. Meidinger, R. Andritschke, W. Bornemann, D. Coutinho, V. Emberger, O. Hälker, W. Kink, B. Micán, S. Müller, D. Pietschner, P. Predehl, J. Reiffers, Report on the eROSITA camera system, in *Society of Photo-Optical Instrumentation Engineers (SPIE) Conference Series*. Society of Photo-Optical Instrumentation Engineers (SPIE) Conference Series, vol. 9144, 2014, p. 1. doi:10.1117/12.2055703
- A. Melandri, B. Sbarufatti, P. D’Avanzo, R. Salvaterra, S. Campana, S. Covino, S.D. Vergani, L. Nava, G. Ghisellini, G. Ghirlanda, D. Fugazza, V. Mangano, M. Capalbi, G. Tagliaferri, The dark bursts population in a complete sample of bright Swift long gamma-ray bursts. *MNRAS* **421**, 1265–1272 (2012). doi:10.1111/j.1365-2966.2011.20398.x
- R.A. Mesler, Y.M. Pihlström, Calorimetry of GRB 030329: Simultaneous Model Fitting to the Broadband Radio Afterglow and the Observed Image Expansion Rate. *ApJ* **774**, 77 (2013). doi:10.1088/0004-637X/774/1/77
- R.A. Mesler, Y.M. Pihlström, G.B. Taylor, J. Granot, VLBI and Archival VLA and WSRT Observations of the GRB 030329 Radio Afterglow. *ApJ* **759**, 4 (2012). doi:10.1088/0004-637X/759/1/4
- P. Mészáros, M.J. Rees, Population III Gamma-ray Bursts. *ApJ* **715**, 967–971 (2010). doi:10.1088/0004-637X/715/2/967
- B.D. Metzger, P.K.G. Williams, E. Berger, Extragalactic Transients in the Era of Wide-Field Radio Surveys. I. Detection Rates and Light Curve Characteristics. *ArXiv e-prints* (2015)
- M.J. Michałowski, A. Kamble, J. Hjorth, D. Malesani, R.F. Reinfrank, L. Bonavera, J.M. Castro Cerón, E. Ibar, J.S. Dunlop, J.P.U. Fynbo, M.A. Garrett, P. Jakobsson, D.L. Kaplan, T. Krühler, A.J. Levan, M. Massardi, S. Pal, J. Sollerman, N.R. Tanvir, A.J. van der Horst, D. Watson, K. Wiersema, The Optically Unbiased GRB Host (TOUGH) Survey. VI. Radio Observations at $z > \sim 1$ and Consistency with Typical Star-forming Galaxies. *ApJ* **755**, 85 (2012). doi:10.1088/0004-637X/755/2/85
- D.A. Perley, R.A. Perley, Radio Constraints on Heavily Obscured Star Formation. *ApJ* **778**, 172 (2013). doi:10.1088/0004-637X/778/2/172
- D.A. Perley, S.B. Cenko, A. Corsi, N.R. Tanvir, A.J. Levan, D.A. Kann, E. Sonbas, K. Wiersema, W. Zheng, X.-H. Zhao, J.-M. Bai, M. Bremer, A.J. Castro-Tirado, L. Chang, K.I. Clubb, D. Frail, A. Fruchter, E. Göğüş, J. Greiner, T. Güver, A. Horesh, A.V. Filippenko, S. Klose, J. Mao, A.N. Morgan, A.S. Pozanenko, S. Schmidl, B. Stecklum, M. Tanga, A.A. Volnova, A.E. Volvach, J.-G. Wang, J.-M. Winters, Y.-X. Xin, The Afterglow of GRB 130427A from 1 to 10^{16} GHz. *ApJ* **781**, 37 (2014). doi:10.1088/0004-637X/781/1/37
- D.A. Perley, R.A. Perley, J. Hjorth, M.J. Michałowski, S.B. Cenko, P. Jakobsson, T. Krühler,

- A.J. Levan, D. Malesani, N.R. Tanvir, Connecting GRBs and ULIRGs: A Sensitive, Unbiased Survey for Radio Emission from Gamma-Ray Burst Host Galaxies at $0.0 < z < 2.5$. *ApJ* **801**, 102 (2015). doi:10.1088/0004-637X/801/2/102
- Y.M. Pihlström, G.B. Taylor, J. Granot, S. Doleman, Stirring the Embers: High-Sensitivity VLBI Observations of GRB 030329. *ApJ* **664**, 411–415 (2007). doi:10.1086/518955
- P. Predehl, R. Andritschke, W. Becker, W. Bornemann, H. Bräuninger, H. Brunner, T. Boller, V. Burwitz, W. Burkert, N. Clerc, E. Churazov, D. Coutinho, K. Dennerl, J. Eder, V. Emberger, T. Eraerds, M.J. Freyberg, P. Friedrich, M. Fürmetz, A. Georgakakis, C. Grossberger, F. Haberl, O. Hälker, G. Hartner, G. Hasinger, J. Hoelzl, H. Huber, A. von Kienlin, W. Kink, I. Kreykenbohm, G. Lamer, I. Lomakin, I. Lapchov, L. Lovisari, N. Meidinger, A. Merloni, B. Mican, J. Mohr, S. Müller, K. Nandra, F. Pacaud, M.N. Pavlinsky, E. Perinati, E. Pfeffermann, D. Pietschner, J. Reiffers, T. Reiprich, J. Robrade, M. Salvato, A.E. Santangelo, M. Sasaki, H. Scheuerle, C. Schmid, J. Schmitt, A.D. Schwobe, R. Sunyaev, C. Tenzer, L. Tiedemann, W. Xu, V. Yaroshenko, S. Walther, M. Wille, J. Wilms, Y.-Y. Zhang, eROSITA on SRG, in *Society of Photo-Optical Instrumentation Engineers (SPIE) Conference Series*. Society of Photo-Optical Instrumentation Engineers (SPIE) Conference Series, vol. 9144, 2014, p. 1. doi:10.1117/12.2055426
- N. Produit, F. Barao, S. Deluit, W. Hajdas, C. Leluc, M. Pohl, D. Rapin, J.-P. Vialle, R. Walter, C. Wigger, POLAR, a compact detector for gamma-ray bursts photon polarization measurements. *Nuclear Instruments and Methods in Physics Research A* **550**, 616–625 (2005). doi:10.1016/j.nima.2005.05.066
- J.L. Racusin, S.V. Karpov, M. Sokolowski, J. Granot, X.F. Wu, V. Pal'Shin, S. Covino, A.J. van der Horst, S.R. Oates, P. Schady, R.J. Smith, J. Cummings, R.L.C. Starling, L.W. Piotrowski, B. Zhang, P.A. Evans, S.T. Holland, K. Malek, M.T. Page, L. Vetere, R. Margutti, C. Guidorzi, A.P. Kamble, P.A. Curran, A. Beardmore, C. Kouveliotou, L. Mankiewicz, A. Melandri, P.T. O'Brien, K.L. Page, T. Piran, N.R. Tanvir, G. Wrochna, R.L. Aptekar, S. Barthelmy, C. Bartolini, G.M. Beskin, S. Bondar, M. Bremer, S. Campana, A. Castro-Tirado, A. Cucchiara, M. Cwiok, P. D'Avanzo, V. D'Elia, M. Della Valle, A. de Ugarte Postigo, W. Dominik, A. Falcone, F. Fiore, D.B. Fox, D.D. Frederiks, A.S. Fruchter, D. Fugazza, M.A. Garrett, N. Gehrels, S. Golenetskii, A. Gomboc, J. Gorosabel, G. Greco, A. Guarnieri, S. Immler, M. Jelinek, G. Kasprowitz, V. La Parola, A.J. Levan, V. Mangano, E.P. Mazets, E. Molinari, A. Moretti, K. Nawrocki, P.P. Oleynik, J.P. Osborne, C. Pagani, S.B. Pandey, Z. Paragi, M. Perri, A. Piccioni, E. Ramirez-Ruiz, P.W.A. Roming, I.A. Steele, R.G. Strom, V. Testa, G. Tosti, M.V. Ulanov, K. Wiersema, R.A.M.J. Wijers, J.M. Winters, A.F. Zarnecki, F. Zerbi, P. Mészáros, G. Chincarini, D.N. Burrows, Broadband observations of the naked-eye γ -ray burst GRB080319B. *Nature* **455**, 183–188 (2008). doi:10.1038/nature07270
- E. Rol, A. van der Horst, K. Wiersema, S.K. Patel, A. Levan, M. Nysewander, C. Kouveliotou, R.A.M.J. Wijers, N. Tanvir, D. Reichart, A.S. Fruchter, J. Graham, J.-E. Ovaldsen, A.O. Jaunsen, P. Jonker, W. van Ham, J. Hjorth, R.L.C. Starling, P.T. O'Brien, J. Fynbo, D.N. Burrows, R. Strom, GRB 051022: Physical Parameters and Extinction of a Prototype Dark Burst. *ApJ* **669**, 1098–1106 (2007). doi:10.1086/521336
- E.M. Rossi, R. Perna, F. Daigne, 'Orphan' afterglows in the Universal structured jet model for γ -ray bursts. *MNRAS* **390**, 675–682 (2008)
- T. Sakamoto, D.Q. Lamb, C. Graziani, T.Q. Donaghy, M. Suzuki, G. Ricker, J.-L. Atteia, N. Kawai, A. Yoshida, Y. Shirasaki, T. Tamagawa, K. Torii, M. Matsuoka, E.E. Fenimore, M. Galassi, T. Tavenner, J. Doty, R. Vanderspek, G.B. Crew, J. Villasenor, N. Butler, G. Prigozhin, J.G. Jernigan, C. Barraud, M. Boer, J.-P. Dezalay, J.-F. Olive, K. Hurley, A. Levine, G. Monnelly, F. Martel, E. Morgan, S.E. Woosley, T. Cline, J. Braga, R. Manchanda, G. Pizzichini, K. Takagishi, M. Yamauchi, High Energy Transient Explorer 2 Observations of the Extremely Soft X-Ray Flash XRF 020903. *ApJ* **602**, 875–885 (2004). doi:10.1086/381232
- R. Salvaterra, High redshift Gamma-Ray Bursts. *Journal of High Energy Astrophysics* **7**, 35–43 (2015). doi:10.1016/j.jheap.2015.03.001
- I. Shivvers, E. Berger, A Beaming-independent Estimate of the Energy Distribution of Long Gamma-Ray Bursts: Initial Results and Future Prospects. *ApJ* **734**, 58 (2011). doi:10.1088/0004-637X/734/1/58
- A.M. Soderberg, S.R. Kulkarni, D.B. Fox, E. Berger, P.A. Price, S.B. Cenko, D.A. Howell, A.

- Gal-Yam, D.C. Leonard, D.A. Frail, D. Moon, R.A. Chevalier, M. Hamuy, K.C. Hurley, D. Kelson, K. Koviak, W. Krzeminski, P. Kumar, A. MacFadyen, P.J. McCarthy, H.S. Park, B.A. Peterson, M.M. Phillips, M. Rauch, M. Roth, B.P. Schmidt, S. Sheckman, An HST Search for Supernovae Accompanying X-Ray Flashes. *ApJ* **627**, 877–887 (2005). doi:10.1086/430405
- M. Sparre, O.E. Hartoog, T. Krühler, J.P.U. Fynbo, D.J. Watson, K. Wiersema, V. D’Elia, T. Zafar, P.M.J. Afonso, S. Covino, A. de Ugarte Postigo, H. Flores, P. Goldoni, J. Greiner, J. Hjorth, P. Jakobsson, L. Kaper, S. Klose, A.J. Levan, D. Malesani, B. Milvang-Jensen, M. Nardini, S. Piranomonte, J. Sollerman, R. Sánchez-Ramírez, S. Schulze, N.R. Tanvir, S.D. Vergani, R.A.M.J. Wijers, The Metallicity and Dust Content of a Redshift 5 Gamma-Ray Burst Host Galaxy. *ApJ* **785**, 150 (2014). doi:10.1088/0004-637X/785/2/150
- G.W. Suarez, PhD thesis, University of Geneva, 2010
- J. Sun, PhD thesis, Graduate University of Chinese Academy of Sciences, 2012
- N.R. Tanvir, P. Jakobsson, Observations of GRBs at high redshift. *Philosophical Transactions of the Royal Society of London Series A* **365**, 1377–1384 (2007). doi:10.1098/rsta.2006.1992
- N.R. Tanvir, D.B. Fox, A.J. Levan, E. Berger, K. Wiersema, J.P.U. Fynbo, A. Cucchiara, T. Krühler, N. Gehrels, J.S. Bloom, J. Greiner, P.A. Evans, E. Rol, F. Olivares, J. Hjorth, P. Jakobsson, J. Farihi, R. Willingale, R.L.C. Starling, S.B. Cenko, D. Perley, J.R. Maund, J. Duke, R.A.M.J. Wijers, A.J. Adamson, A. Allan, M.N. Bremer, D.N. Burrows, A.J. Castro-Tirado, B. Cavanagh, A. de Ugarte Postigo, M.A. Dopita, T.A. Fatkhullin, A.S. Fruchter, R.J. Foley, J. Gorosabel, J. Kennea, T. Kerr, S. Klose, H.A. Krimm, V.N. Komarova, S.R. Kulkarni, A.S. Moskvitin, C.G. Mundell, T. Naylor, K. Page, B.E. Penprase, M. Perri, P. Podsiadlowski, K. Roth, R.E. Rutledge, T. Sakamoto, P. Schady, B.P. Schmidt, A.M. Soderberg, J. Sollerman, A.W. Stephens, G. Stratta, T.N. Ukwatta, D. Watson, E. Westra, T. Wold, C. Wolf, A γ -ray burst at a redshift of $z \sim 8.2$. *Nature* **461**, 1254–1257 (2009). doi:10.1038/nature08459
- N.R. Tanvir, A.J. Levan, A.S. Fruchter, J.P.U. Fynbo, J. Hjorth, K. Wiersema, M.N. Bremer, J. Rhoads, P. Jakobsson, P.T. O’Brien, E.R. Stanway, D. Bersier, P. Natarajan, J. Greiner, D. Watson, A.J. Castro-Tirado, R.A.M.J. Wijers, R.L.C. Starling, K. Misra, J.F. Graham, C. Kouveliotou, Star Formation in the Early Universe: Beyond the Tip of the Iceberg. *ApJ* **754**, 46 (2012). doi:10.1088/0004-637X/754/1/46
- G.B. Taylor, D.A. Frail, E. Berger, S.R. Kulkarni, The Angular Size and Proper Motion of the Afterglow of GRB 030329. *ApJL* **609**, 1–4 (2004). doi:10.1086/422554
- A.J. van der Horst, Z. Paragi, A.G. de Bruyn, J. Granot, C. Kouveliotou, K. Wiersema, R.L.C. Starling, P.A. Curran, R.A.M.J. Wijers, A. Rowlinson, G.A. Anderson, R.P. Fender, J. Yang, R.G. Strom, A comprehensive radio view of the extremely bright gamma-ray burst 130427A. *MNRAS* **444**, 3151–3163 (2014). doi:10.1093/mnras/stu1664
- H. van Eerten, A. van der Horst, A. MacFadyen, Gamma-Ray Burst Afterglow Broadband Fitting Based Directly on Hydrodynamics Simulations. *ApJ* **749**, 44 (2012)
- J. van Paradijs, P.J. Groot, T. Galama, C. Kouveliotou, R.G. Strom, J. Telting, R.G.M. Rutten, Fishman, Transient optical emission from the error box of the γ -ray burst of 28 February 1997. *Nature* **386**, 686–689 (1997)
- F.Y. Wang, V. Bromm, T.H. Greif, A. Stacy, Z.G. Dai, A. Loeb, K.S. Cheng, Probing Pre-galactic Metal Enrichment with High-redshift Gamma-Ray Bursts. *ApJ* **760**, 27 (2012). doi:10.1088/0004-637X/760/1/27
- H. Wolter, Spiegelsysteme streifenden einfalls als abbildende optiken für röntgenstrahlen. *Annalen der Physik* **445**(1-2), 94–114 (1952). doi:10.1002/andp.19524450108. <http://dx.doi.org/10.1002/andp.19524450108>
- P.R. Wozniak, S.R. Kulkarni, J. Bloom, N. Brandt, D. Fox, A. Gal-Yam, N. Gehrels, L. Jones, M. Kasliwal, C. Kouveliotou, E. Nakar, A. Rau, M. Strauss, W.T. Vestrand, Explosive Transients in the Distant Universe, in *astro2010: The Astronomy and Astrophysics Decadal Survey*. ArXiv Astrophysics e-prints, vol. 2010, 2009, p. 326
- S. Xiong, N. Produit, B. Wu, Expected performance of a hard X-ray polarimeter (POLAR) by Monte Carlo simulation. *Nuclear Instruments and Methods in Physics Research A* **606**, 552–559 (2009). doi:10.1016/j.nima.2009.04.033

-
- D. Yonetoku, T. Murakami, S. Gunji, T. Mihara, K. Toma, T. Sakashita, Y. Morihara, T. Takahashi, N. Toukairin, H. Fujimoto, Y. Kodama, S. Kubo, IKAROS Demonstration Team, Detection of Gamma-Ray Polarization in Prompt Emission of GRB 100826A. *ApJL* **743**, 30 (2011). doi:10.1088/2041-8205/743/2/L30
- W. Yuan, C. Zhang, H. Feng, S.N. Zhang, Z.X. Ling, D.H. Zhao, J. Deng, Y.L. Qiu, J.P. Osborne, P. O'Brien, R. Willingale, J.S. Lapington, Einstein Probe - a small mission to monitor and explore the dynamic X-ray Universe, in *Proceedings of Swift: 10 Years of Discovery (SWIFT 10), held 2-5 December 2014 at La Sapienza University, Rome, Italy. id.6, arXiv:1506.07735*, 2015, p. 6
- B. Zhang, Gamma-Ray Burst Prompt Emission. *International Journal of Modern Physics D* **23**, 30002 (2014). doi:10.1142/S021827181430002X
- D. Zhao, C. Zhang, W. Yuan, R. Willingale, Z. Ling, H. Feng, H. Li, J. Ji, W. Wang, S. Zhang, Ray tracing simulations for the wide-field x-ray telescope of the Einstein Probe mission based on Geant4 and XRTG4, in *Society of Photo-Optical Instrumentation Engineers (SPIE) Conference Series*. Society of Photo-Optical Instrumentation Engineers (SPIE) Conference Series, vol. 9144, 2014, p. 4. doi:10.1117/12.2055434